J. Fluid Mech. (2023), *vol*. 974, A45, doi:10.1017/jfm.2023.739

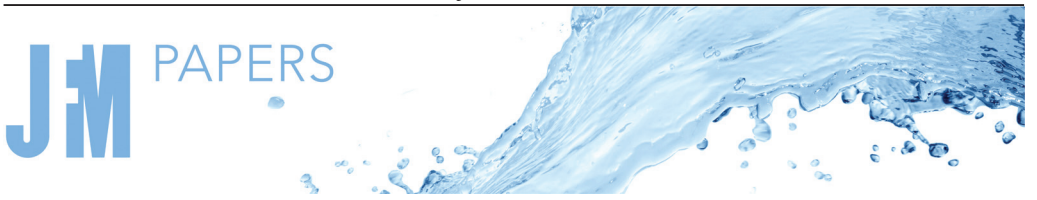

A new propulsion enhancement mechanism in metachronal rowing at intermediate Reynolds numbers

Seth Lionetti[1], Zhipeng Lou[1], Adrian Herrera-Amaya[2], Margaret L. Byron[2] and Chengyu Li[1,†]

[1]Department of Mechanical Engineering, Villanova University, Villanova, PA 19085, USA

[2]Department of Mechanical Engineering, Pennsylvania State University, University Park, PA 16802, USA

(Received 10 November 2022; revised 19 May 2023; accepted 1 September 2023)

Metachronal rowing is a biological propulsion mechanism employed by many swimming invertebrates (e.g. copepods, ctenophores, krill and shrimp). Animals that swim using this mechanism feature rows of appendages that oscillate in a coordinated wave. In this study, we used observations of a swimming ctenophore (comb jelly) to examine the hydrodynamic performance and vortex dynamics associated with metachronal rowing. We first reconstructed the beating kinematics of ctenophore appendages based on a high-speed video of a metachronally coordinated row. Following the reconstruction, two numerical models were developed and simulated using an in-house immersed-boundary-method-based computational fluid dynamics solver. The two models included the original geometry (16 appendages in a row) and a sparse geometry (8 appendages, formed by removing every other appendage along the row). We found that appendage tip vortex interactions contribute to hydrodynamic performance via a vortex-weakening mechanism. Through this mechanism, appendage tip vortices are significantly weakened during the drag-producing recovery stroke. As a result, the swimming ctenophore produces less overall drag, and its thrust-to-power ratio is significantly improved (up to 55.0 % compared with the sparse model). Our parametric study indicated that such a propulsion enhancement mechanism is less effective at higher Reynolds numbers. Simulations were also used to investigate the effects of substrate curvature on the unsteady hydrodynamics. Our results illustrated that, compared with a flat substrate, arranging appendages on a curved substrate can boost the overall thrust generation by up to 29.5 %. These findings provide new insights into the fluid dynamic principles of propulsion enhancement underlying metachronal rowing.

Key words: propulsion, swimming/flying

† Email address for correspondence: chengyu.li@villanova.edu

1. Introduction

Metachronal rowing is commonly found among small swimming invertebrates, such as copepods, ctenophores, krill and shrimp. Animals that locomote via this mechanism feature rows of appendages that oscillate in a coordinated wave. This metachronal wave is induced by a phase lag between adjacent appendages, and it propagates through the row as the appendages oscillate. The beat cycle of each individual appendage consists of a power stroke and a recovery stroke. The power stroke produces thrust, while the recovery stroke generates a certain amount of drag (Sleigh 1976). During the power stroke, the appendage remains fairly straight and sweeps in the direction opposite to the body's motion; during the recovery stroke, it bends and returns to its original position. Figure 1 shows the power stroke and recovery stroke of a row of appendages (e.g. cilia) engaged in metachronal motion.

1.1. *Hydrodynamic performance*

Previous studies have identified several factors that influence the performance of metachronal-rowing-based propulsion. Such factors include (but are not limited to) beat frequency, number of appendages and phase lag between adjacent appendages (Murphy *et al.* 2011; Byron *et al.* 2021). By altering the flow in the vicinity of each appendage, these factors can modify fluid displacement and the associated hydrodynamic performance. Barlow & Sleigh (1993) studied the effects of beat frequency of a ctenophore's rowing appendages (ctenes) on the water propulsion speeds. They observed that, as beat frequency increases, the propagation velocity of the metachronal wave increases, and the phase lag between adjacent ctenes (expressed as a percentage of the total cycle time) also increases. As a consequence, the water flow speed increases proportional to the appendage tip speed, and the power output of the metachronal wave increases exponentially. Another factor that can modify flow transport of metachronal rowing is the number of appendages. Gueron & Levit-Gurevich (1999) modelled ciliary propulsion using various numbers of beating appendages. They showed that the efficiency of metachronal rowing improves as the number of appendages increases. While this analysis is only valid for very low Reynolds numbers ($Re \ll 1$, where $Re \equiv UL/\nu$ with U as a representative velocity scale, L a representative length scale and ν the fluid kinematic viscosity), it suggests that interactions between rowing appendages are likely to enhance the hydrodynamic performance of metachronal rowing. Colin *et al.* (2020) studied several species that swim at much higher Re, including ctenophores, annelid worms and arthropods. They found that these metachronal swimmers generate thrust by producing negative pressure along the leeward side of their appendages. This phenomenon, called 'suction thrust', is a result of the bending kinematics of the rowing appendages.

Another key factor that influences the hydrodynamic performance of metachronal rowing is the phase lag between appendages. To examine the effects of phase lag, Alben *et al.* (2010) compared a krill's metachronal kinematics with synchronous kinematics, in which the phase lag is zero. They observed that metachronal rowing results in a higher average body speed. Ford & Santhanakrishnan (2021*b*) reached a similar conclusion through particle image velocimetry measurements of a robotic krill. They also noticed that, when a phase lag is introduced, the robotic krill's body velocity decreases as appendages move toward each other and increases as they move apart. This finding further indicates that the performance benefits of metachronal rowing are due to hydrodynamic interactions between appendages.

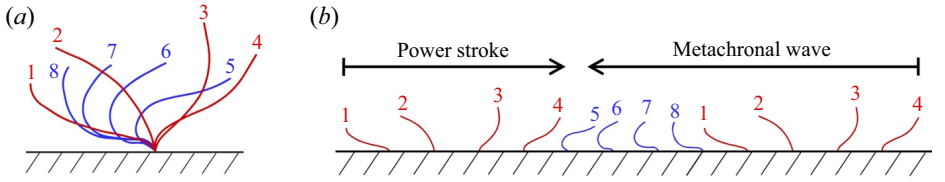

Figure 1. Diagram showing (*a*) the beat cycle of a single rowing appendage (e.g. a cilium) and (*b*) a row of appendages oscillating together in a coordinated metachronal wave. The power stroke is shown in red, and the recovery stroke is shown in blue. In this figure, the direction of the metachronal wave is opposite to the direction of the appendages' power stroke, which indicates that the wave is antiplectic (Knight-Jones 1954).

1.2. *Vortex interactions*

For all forms of drag-based paddling at sufficiently high Reynolds numbers, an appendage generates tip vortices over one beat cycle that contribute to thrust generation (Kim & Gharib 2011). As appendages beat in a metachronal wave, these tip vortices interact in various ways that influence hydrodynamic performance. In general, vortex interactions can be characterized as either constructive or destructive (Gopalkrishnan *et al.* 1994). Vortices are strengthened by constructive interactions, and they are weakened or destroyed by destructive interactions. Only a few previous studies have examined the tip vortex interactions that occur during metachronal rowing. Ford & Santhanakrishnan (2021*a*) used a simplified two-link model to study krill propulsion ($Re \approx 300$). By decreasing the distance between adjacent appendages, they found that counterrotating tip vortices merge to form a horizontally oriented wake, thereby improving the hydrodynamic performance of metachronal rowing. In another study, Garayev & Murphy (2021) examined the tip vortex interactions among a mantis shrimp's pleopods. They identified a mechanism in which the vortex formed by the anteriormost pleopod pair is intercepted and strengthened by the posteriormost pleopod pair. This mechanism improves the mantis shrimp's swimming speed and efficiency, but the authors note that it is likely effective only at relatively high Reynolds numbers ($Re \approx 5000$). This is because at low Reynolds numbers ($Re < 100$), tip vortices do not readily shed into the wake. Granzier-Nakajima, Guy & Zhang-Molina (2020) showed that, at low Re (≈ 1), tip vortices remain attached to an appendage throughout its beat cycle. They also demonstrated that as Re increases and inertial forces increasingly dominate ($Re \approx 100$), tip vortices tend to detach from the beating appendages. To examine tip vortex interactions at intermediate Reynolds numbers, Dauptain, Favier & Bottaro (2008) ran numerical simulations of ctenophore swimming ($Re \approx 50$). By artificially increasing the distance between adjacent appendages, they showed that as the distance increases, the thrust-to-power ratio of the appendages decreases. This observation supports the hypothesis that tip vortex interactions enhance hydrodynamic performance. However, the exact propulsion enhancement mechanism of such attached tip vortex interactions remains unknown.

1.3. *Variation of size and shape*

In nature, metachronal-rowing-based propulsion can be found in a wide variety of species, ranging in size from paramecia (body-scale $Re \approx 0.2$) (Zhang *et al.* 2015) to lobsters (body-scale $Re \approx 7500$) (Lim & DeMont 2009). Among these species, ctenophores (body-scale $Re \approx 100$–6000) are the largest animals that locomote using cilia, which beat with an appendage-scale Re of 10–300 (Matsumoto 1991). Unlike larger metachronal appendages such as those found in krill (Murphy *et al.* 2011) and lobsters (Lim &

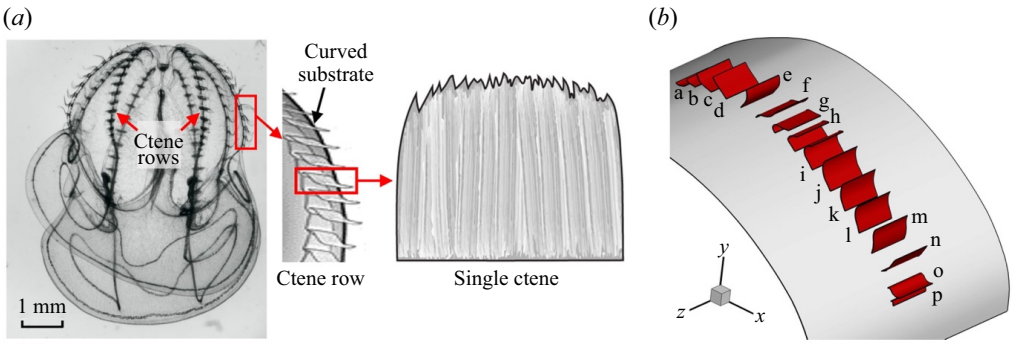

Figure 2. Comparison between (*a*) the real ctenophore body and (*b*) the ctene row reconstruction. The ctenophore body is lined by eight ctene rows. Each row consists of sixteen ctenes situated along a curved substrate, and each ctene contains thousands of individual cilia. The reconstructed model ctene row consists of sixteen rectangular ctene meshes situated along a curved rectangular substrate mesh. The substrate mesh is coloured grey, and the sixteen ctenes are coloured red and are labelled alphabetically.

DeMont 2009), ctenophore cilia are fully flexible and therefore exhibit different bending kinematics. Ctenophore therefore present a unique opportunity to study the vortex dynamics of ciliary propulsion, a common biological propulsion system used across the low-to-intermediate Reynolds number regime. As shown in figure 2, ctenophores have eight rows containing multiple appendages called ctenes, and each ctene consists of thousands of long (*mm*-scale) cilia fused together (Afzelius 1961). Several previous studies have explored the relationship between *Re* and ctenophore hydrodynamic performance. Barlow, Sleigh & White (1993) increased *Re* for a swimming ctenophore by adjusting its ctene beating frequency. They found that, as *Re* increases, high-speed flow detaches from the ctene tip and is shed into the flow stream. In a separate study, Herrera-Amaya *et al.* (2021) examined how varying *Re* affects the spatio-temporal asymmetry of ctene kinematics. Their results showed that increasing *Re* is associated with a quicker power stroke and slower recovery stroke. In addition, the spatial asymmetry of ctene beating is reduced as *Re* increases. However, for very low *Re* ($Re \ll 1$), symmetry must be broken in order to produce net flow. Takagi (2015) demonstrated that in time-reversible flow conditions ($Re \ll 1$), it is possible to generate thrust using a spatially symmetric stroke, as long as a phase lag is introduced between adjacent appendages. These findings indicate that varying *Re*, together with hydrodynamic interactions between appendages, strongly influence ctene kinematics and hydrodynamic performance. However, it is unclear how *Re* affects the inter-ctene flow interactions that occur during ctenophore swimming.

Apart from their beating kinematics, ctenophores are also noteworthy for their diverse body morphologies. Depending on the species, ctenophores may possess lobate, oblong, roughly spherical or even ribbon-like bodies (Tamm 2014; Gibbons *et al.* 2021). Despite this natural diversity of body shapes, previous studies on metachronal propulsion (as well as the large body of literature on ciliary flow) have largely assumed the substrate geometry is completely flat (Dauptain *et al.* 2008; Elgeti & Gompper 2013; Granzier-Nakajima *et al.* 2020; Ford & Santhanakrishnan 2021*a*). It is therefore unknown how substrate curvature impacts the hydrodynamic performance of metachronal rowing and the inter-ctene flow interactions.

To address the aforementioned gaps in knowledge, the present study employs an in-house immersed-boundary-method-based computational fluid dynamics (CFD) solver to simulate metachronal rowing. We first reconstructed the beating kinematics of

ctenophore ctenes in a row (16 ctenes) based on high-speed video of a forward-swimming ctenophore. In addition to the original reconstructed geometry, we created a sparse model (8 ctenes) by removing every other ctene along the row. We then conducted a comprehensive parametric study to investigate the flow interactions of ctenophore appendages and the effects of substrate geometry on the unsteady hydrodynamics of metachronal rowing. Simulation results were used to calculate force generation and hydrodynamic power consumption for each ctene, as well as vorticity and wake structures for the entire row. Using these results, we aim to answer three questions: (i) how ctene tip vortex interactions affect hydrodynamic performance, (ii) how varying *Re* affects tip vortex interactions and (iii) how varying substrate curvature affects ctene row hydrodynamics.

2. Methodology

2.1. *Morphological model*

A high-speed recording system was used to capture real beating kinematics of ctenophore ctenes. Ctenophores were placed inside a transparent filming vessel, and the vessel was illuminated using a collimated LED light source. Three high-speed cameras and 200 mm macro lenses were used to record the swimming ctenophore. Images were captured at 600 frames per second. This set-up is described in detail by Karakas, Maas & Murphy (2020), whose data are contemporary.

We collected 27 separate recordings of free-swimming ctenophores using the multicamera high-speed video set-up. These videos were then examined carefully, and one recording was selected for further study; in the selected recording, the ctenophore was swimming unidirectionally at an approximately constant speed, and the image acquisition was high quality for model reconstruction (the ctenes themselves were orthogonal to the plane of focus over the duration of the recording, with the beating direction in plane). The selected high-speed video was then imported into Autodesk Maya, where it was used to create a meshed model of a single ctene row. The model ctene row, shown in figure 2, consists of sixteen ctenes (labelled ‘a’ to ‘p’) situated along a curved rectangular substrate. In nature, each ctene contains thousands of cilia that are grouped into a paddle-like structure, whose thickness is very small compared with its length and width (Afzelius 1961). Although ctenes include many individual cilia, they function as hydrodynamically solid surfaces (Goebel *et al.* 2020). Therefore, in this study, ctenes are modelled as rectangular membrane surfaces. As observed in the real ctenophore, larger ctenes are located near the middle of the row. In addition, the curvature of the model substrate matches the ctenophore’s body curvature in the beating plane. Because we created the reconstruction based on a side-view video of the ctene row, we do not consider curvature in the plane normal to the beating plane. In our model, the substrate must be wide enough to capture real flow interactions between the ctenes and substrate. In order to achieve this, the ratio of substrate width to ctene width is 6 : 1. Details regarding ctene dimensions are included in Appendix A.

To reconstruct the swimming kinematics of the ctene row for one beat cycle, a side-view orientation of the model row was superimposed over the high-speed video of the swimming ctenophore. Then, the model ctenes were aligned with various frames of the video. Because the reconstruction was created using a side view of the ctene row, the bending of each model ctene does not vary along its width. Between the frames used for reconstruction, seven-term Fourier interpolation was used to interpolate the surface mesh over time, producing a high temporal frequency (960 time steps per beat cycle) input for our CFD solver. Figure 3 compares the reconstruction with images of the real ctenophore.

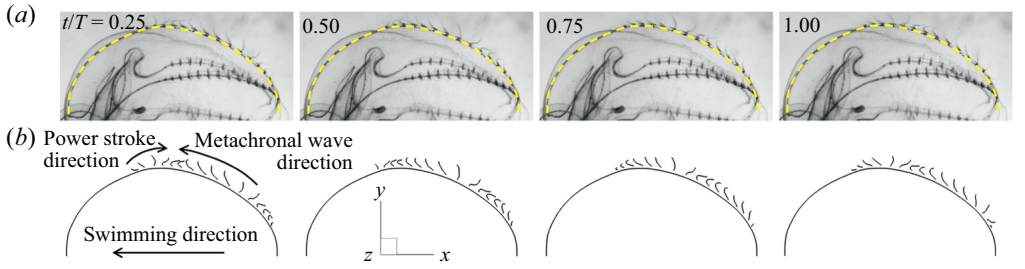

Figure 3. Time sequence of a metachronal wave propagating through the real ctene row (*a*) as well as the row reconstruction (*b*) over one beat cycle *T*. The power stroke direction, metachronal wave direction and ctenophore swimming direction are labelled. In the images showing the real ctene row, the body curvature is highlighted using a yellow dashed line.

Both the reconstruction and the real ctenophore exhibit a metachronal wave that travels through the ctene row as the beat cycle progresses. The direction of the metachronal wave is opposite to the direction of the ctenes' power stroke (antiplectic) (Knight-Jones 1954). In addition, the axes used in this study are defined in the second panel of figure 3. The *x*-axis extends in the direction opposite to the ctenophore's swimming direction, the *y*-axis points above the ctenophore's body and the *z*-axis extends out of the plane.

2.2. *Ctenophore swimming kinematics*

The ctenophore used in this study has a body length (L_b) of 11.56 mm. The average ctene length (l) along the row is 0.62 mm, with a standard deviation of 0.02 mm. The ctene stroke amplitude (averaged over all sixteen ctenes in the row) is 100.50°, defined as the angle traced by the ctene tip during the power stroke. The definitions of these morphological parameters are shown in figure 4. In our high-speed video recording, the ctenophore has an approximately constant forward body velocity (U_b) of 7.35 mm s^{-1}. The ctenes have a beating frequency (f) of 13.04 Hz over the selected beat cycle. The ctenes beat sequentially in metachronal motion, with a constant phase lag. The phase lag (P_L) is defined as the average time delay between the beat cycles of adjacent ctenes and is expressed as a percentage of the overall cycle time. The value of P_L is 11.20 % in our recording. More details related to the calculation of stroke amplitude and phase lag are included in Appendix B. The tip trajectories of the reconstructed row of ctenes are shown in figure 5. From the figure, we can clearly tell that the ctenes are situated on a significantly curved substrate. The average body substrate curvature (κ) is 161.51 m^{-1}, which is defined as $1/R$, where R is the radius of the curved substrate. Because the substrate is not perfectly circular, we used a least-squares circle-fitting function to calculate R (Pratt 1987). We fit a circle along the region of the curved substrate occupied by the ctenes (shown in figure 4), and we calculated the curvature R of this circle. Along the length of the substrate, curvature varied from a minimum of 160.77 m^{-1} to a maximum of 162.74 m^{-1}. As shown in figures 3 and 5, the ctenes are located primarily along the back half of the ctenophore's body. The distance of the first and last ctenes from the front edge of the curved body is labelled in figure 5. In addition, we evaluated the ctene tip velocity, computed as $U_{tip} = \sqrt{u_{tip}^2 + v_{tip}^2 + w_{tip}^2}$ where u_{tip}, v_{tip} and w_{tip} are ctene tip velocity components in the x, y and z directions, respectively (w_{tip} is assumed to be zero). Figure 6 shows the average tip velocity U_{tip} for the ctenes. The power stroke is shaded grey and constitutes approximately half of the total beat cycle; it is defined as the elapsed time between the

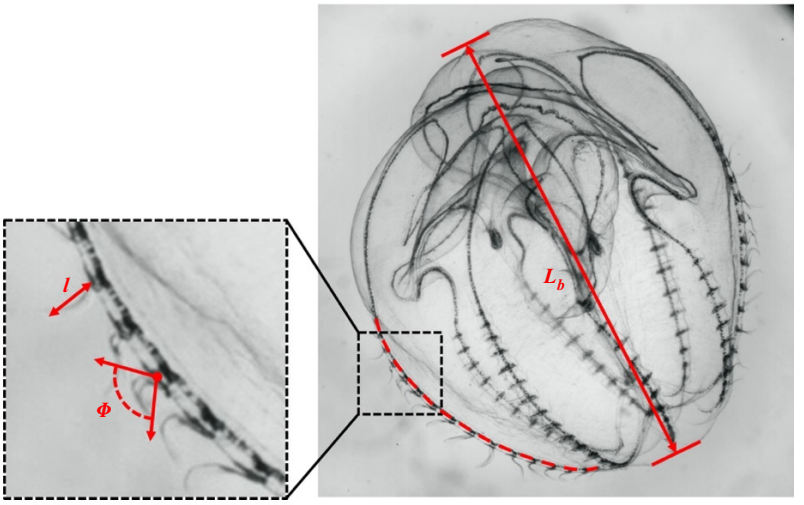

Figure 4. Diagram showing ctenophore body length (L_b), ctene length (l) and stroke amplitude (Φ). The red dashed line in the right image indicates the region over which the body curvature was calculated.

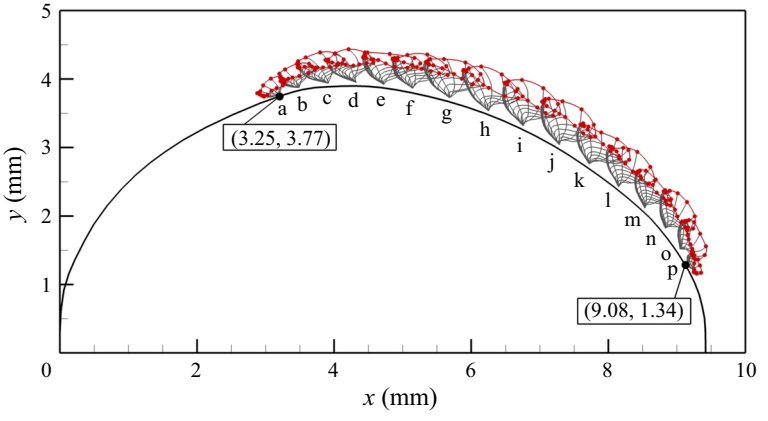

Figure 5. Diagram showing the tip trajectories of the model ctenes. Each ctene is plotted at sixteen instances throughout one beat cycle. The ctene tip is represented using a red circle, and the tip trajectory is traced in red. The instances are spaced equally in time. Axes show the location of the ctenes in relation to the front edge of the curved body. The locations of the first and last ctenes are labelled.

two local minima shown (Herrera-Amaya *et al.* 2021). Morphological and kinematic measurements of the ctenophore used in this study are summarized in table 1. These values are consistent with previous studies on similarly sized ctenophores (Herrera-Amaya *et al.* 2021). In addition, a Fourier-series-least-squares approximation (Blake 1972) of the ctene kinematics is included in Appendix C, which can be used for replication and validation of our results. While the kinematics for this study were prescribed via a frame-by-frame reconstruction of the behavioural experiments, the approximation in Appendix C closely matches what is used here.

As a ctenophore swims, the flow around its body differs from the oscillatory flow produced by each individual ctene. To account for this difference, we define two Reynolds numbers. The body Reynolds number ($Re_b = U_b L_b/\nu$) describes the flow around a

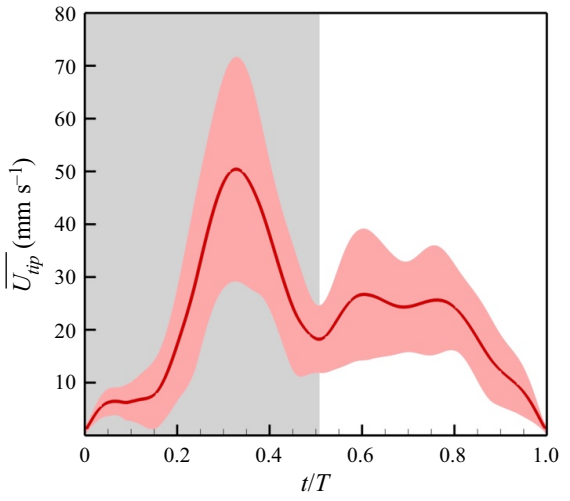

Figure 6. Time course of the ctenes' tip velocity. The solid red curve is the tip velocity, averaged over all sixteen ctenes after removing the phase shift. The pink shaded margins represent the standard deviation of the tip velocity. The power stroke is shaded in grey.

L_b (mm)	κ (m^{-1})	U_b (mm s^{-1})	l (mm)	P_L (%)	Φ (deg.)	f (Hz)
9.43	161.51	7.35	0.62 ± 0.02	11.20	100.50	13.04

Table 1. Morphological and kinematic measurements of the ctenophore used in this study.

ctenophore's body as it swims in a particular direction (where ν, the kinematic viscosity of seawater, is around 1.05 mm^2 s^{-1}). Following the previous literature (Herrera-Amaya *et al.* 2021), the oscillatory Reynolds number ($Re_\omega = 2\pi f l^2/\nu$) is also used to describe flow around each ctene. Based on the measured data in table 1, Re_b is 66.01, and Re_ω is 30.00. These Reynolds numbers are intermediate, which indicates that both viscous and inertial forces play a role in ctenophore propulsion.

2.3. *Numerical method and simulation set-up*

Because both viscous and inertial forces are important for the ctene propulsion, this study employs an immersed-boundary-method-based in-house CFD solver to numerically solve the three-dimensional viscous incompressible Navier–Stokes equations. The non-dimensional form of these equations can be written as

$$\frac{\partial u_i}{\partial x_i} = 0, \quad \frac{\partial u_i}{\partial t} + \frac{\partial (u_i u_j)}{\partial x_j} = -\frac{\partial p}{\partial x_i} + \frac{1}{Re}\frac{\partial}{\partial x_j}\left(\frac{\partial u_i}{\partial x_j}\right), \tag{2.1}$$

where u_i are the velocity components, p is the pressure and Re is the Reynolds number.

The above equations are discretized using a cell-centred collocated grid arrangement of the primitive variables (u_i and p). The fractional step method is used to integrate the equations in time, and a second-order central difference scheme is used in space. An immersed-boundary-method-based approach is applied to handle the complex moving boundaries of the beating ctenes. In this method, boundary conditions are

imposed on the immersed boundaries through a ghost-cell procedure. Compared with boundary-conforming methods, such as curvilinear grid (Visbal & Gaitonde 2001, 2002; Visbal & Rizzetta 2002) and finite-element methods (Tezduyar 2004; Tezduyar *et al.* 2006; Löhner 2008), the immersed-boundary-method approach eliminates the need for complicated re-meshing algorithms. It thus significantly reduces the computational cost associated with simulating flow past complex moving boundaries. Immersed-boundary methods can be broadly divided into two categories: the continuous forcing approach (Peskin 1972; Goldstein, Handler & Sirovich 1993; Taira & Colonius 2007) and the discrete forcing approach (Ye *et al.* 1999; Kim, Kim & Choi 2001; Dong *et al.* 2010). The present study employs a multi-dimensional 'ghost-cell' methodology to impose the boundary conditions on the immersed boundary (Mittal *et al.* 2008). This method can be categorized as a discrete forcing approach, wherein forcing is directly incorporated into the discretized Navier–Stokes equations (Mittal & Iaccarino 2005). The movement of the immersed boundaries (ctenes) were prescribed according to the image-based reconstruction as described in § 2.1. This immersed-boundary method has successfully been used to simulate insect flight (Li, Dong & Zhao 2018, 2020; Li 2021; Lionetti, Hedrick & Li 2022) and bio-inspired propulsion (Li & Dong 2016; Li *et al.* 2019; Li, Dong & Cheng 2020; Lei, Crimaldi & Li 2021). Validations of the current in-house CFD solver can be found in our previous studies (Li, Dong & Liu 2015; Li & Dong 2017; Li *et al.* 2017; Lei & Li 2020). In addition, as seen in Appendix D, our current CFD results are consistent with previous experimental measurements reported by Barlow & Sleigh (1993) and Colin *et al.* (2020), which further proves the validity of the current CFD solver.

Figure 7 shows a schematic of the computational grid and boundary conditions employed in this study. The meshed ctene row was situated at the bottom of a non-uniform Cartesian computational grid that contained two defined layers. The ctene row was located within a very high-density region, and this region was surrounded by a secondary dense layer. Beyond this secondary layer, the grid was stretched rapidly. A constant velocity inflow was specified at the front of the fluid domain, representing the constant swimming speed, and an outflow boundary condition was applied at the back of the domain. All remaining boundaries were assigned a zero-gradient boundary condition. To achieve a periodic stage, simulations were run for four ctene beat cycles; the kinematics of each beat cycle were identical. By inspecting the time history of the force coefficients, we found that in all simulation cases, the flow reaches a nearly periodic state after two beat cycles. Results presented in this paper are based on the fourth cycle.

We performed a parametric study to evaluate how ctene tip vortex interactions, Reynolds number and substrate curvature affect the hydrodynamic performance of a forward-swimming ctenophore. To study the effects of tip vortex interactions, we created a sparse ctene row model that features a greater distance between appendages. This increased distance enabled the observation of ctene hydrodynamics with minimum effects of vortex interactions. The sparse row was a modification of the original reconstruction, formed by removing every other ctene along the row while preserving the original kinematics. The original row and sparse row are compared in figure 8. To evaluate the hydrodynamics of ctene rows across different flow regimes, we simulated kinematics at different Reynolds numbers ($7.5 < Re_\omega < 120$) by adjusting the kinematic viscosity in our simulation set-up. To examine the effects of substrate curvature, we progressively flattened the model substrate used in this study. The details of how we flattened the curved substrate are documented in Appendix E. While keeping other parameters the same, we ran simulations using four different substrate curvatures, including the original curvature,

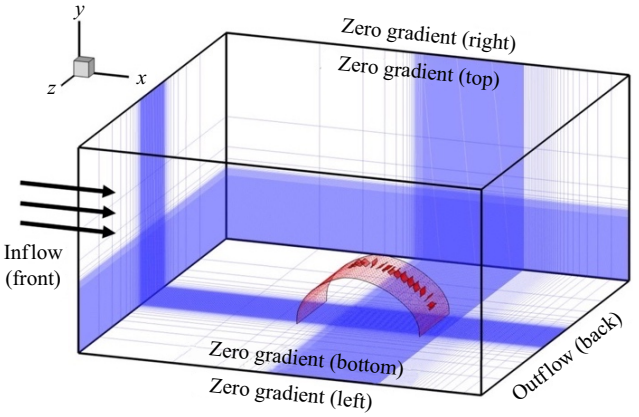

Figure 7. Schematic of the computational grid and boundary conditions used in this study. The computational grid is of size $352 \times 210 \times 114$. The model ctene row consists of a curved rectangular substrate and sixteen rectangular ctene meshes, and it contains approximately 7000 triangle elements.

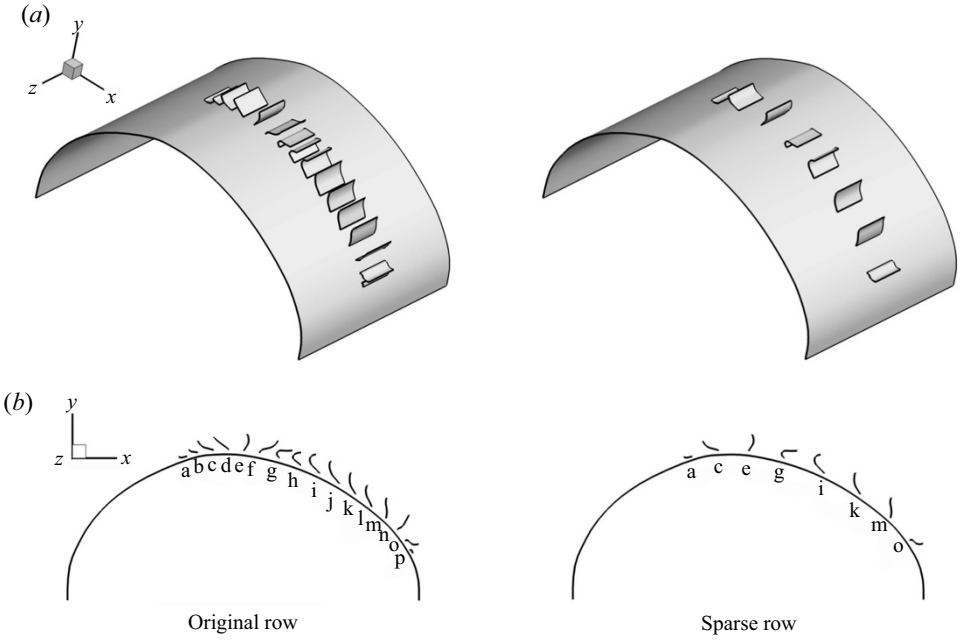

Figure 8. Perspective view (*a*) and side view (*b*) of the original and sparse ctene rows.

medium curvature, low curvature and flat. These substrate geometries are compared in figure 9, and their calculated curvatures are listed in table 2. Table 3 provides a concise summary of all the parameters involved and their range of variation.

To evaluate hydrodynamic performance, we obtained the surface pressure and shear stress distributions along the ctene surfaces by solving the Navier–Stokes equations. Then, we calculated the instantaneous aerodynamic forces by integrating the pressure and shear stress along the surface of the model ctenes. The instantaneous lift F_L and thrust F_T were determined by projecting the integrated force onto the vertical and horizontal directions, respectively. In this paper, forces are presented as non-dimensional coefficients, which are

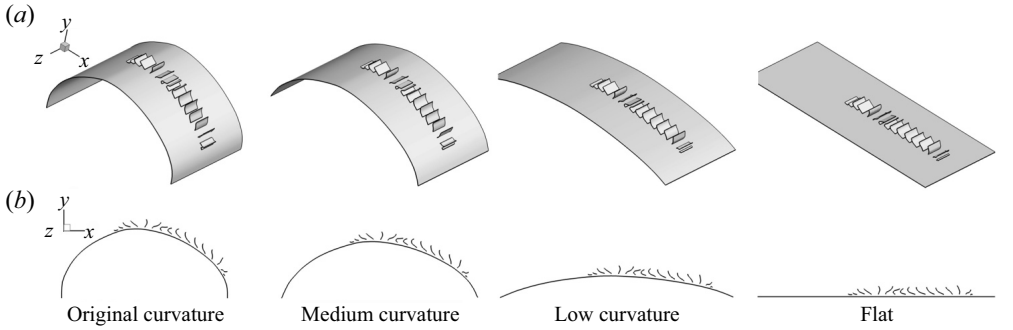

Figure 9. Perspective view (*a*) and side view (*b*) of the different substrate geometries. (Original spacing is shown; curvature variation was also explored with the sparse row.)

	Substrate curvature (m^{-1})
Original curvature	161.51
Medium curvature	119.65
Low curvature	41.20
Flat	0.00

Table 2. Calculated curvature for each substrate geometry.

	Re_ω	Substrate curvature
Original row	7.5, 15, 30, 60, 120	Flat, low, medium, original
Sparse row	7.5, 15, 30, 60, 120	Flat, low, medium, original

Table 3. Summary of different cases involved in the parametric study.

computed as $C_L = F_L/0.5\rho U_{tip}^2 S$ and $C_T = F_T/0.5\rho U_{tip}^2 S$. Here, C_L and C_T represent the lift and thrust coefficients, U_{tip} is the ctene tip velocity, averaged over all ctenes in the row and S denotes the area of the ctene surface, averaged over all ctenes in the row. The total force coefficient is then calculated by $C_F = \sqrt{C_L^2 + C_T^2}$. The instantaneous hydrodynamic power ($P_{hydro} = \oint -(\bar{\bar{\boldsymbol{\sigma}}} \cdot \boldsymbol{n}) \cdot \boldsymbol{V}\, \mathrm{d}s$) is defined as the rate of output work done by the ctene model, where $\oint$ denotes the integration along the model surface, $\bar{\bar{\boldsymbol{\sigma}}}$ and $\boldsymbol{V}$ represent the stress tensor and the velocity vector of the fluid adjacent to the model surface and $\boldsymbol{n}$ is the normal vector of each triangular element on the model surface. Its non-dimensional coefficient (C_{PW}) is calculated as $C_{PW} = P_{hydro}/0.5\rho U_{tip}^3 S$. The immersed-boundary method employed in this study (Mittal *et al.* 2008) is well suited for calculating the aero/hydrodynamic performance of membranous surfaces such as ctenophore ctenes. This method has previously been used to simulate flapping membranous wings (Li *et al.* 2018; Li 2021; Lionetti *et al.* 2022).

3. Results and discussion

In this section, the hydrodynamic performance of a ctene row is evaluated in conditions similar to a typical forward-swimming ctenophore. Ctene thrust generation and tip vortex formation are discussed in detail. To determine the effects of tip vortex interactions, the original reconstruction is compared with a modified sparse ctene row. In addition, ctene performance and vortex structures are presented for different values of Re ($7.5 < Re_\omega < 120$). Finally, effects of substrate curvature are also discussed.

3.1. *Ctene hydrodynamics*

The in-house CFD solver was used to evaluate the hydrodynamic performance of the ctene row reconstruction shown in figure 2, as outlined in § 2.3. The time-varying instantaneous thrust produced by each of the sixteen ctenes is displayed in figure 10. Figure 10(*a*) shows the thrust generated by ctenes 'a'–'d', which are located at the front of the row (see figure 5). This force history provides insight into how ctene bending kinematics influence thrust generation throughout the beat cycle. During the power stroke, thrust peaks as the ctene straightens and sweeps forward. During the recovery stroke, some drag is generated as the ctene deforms and returns to its original position. Due to the spatio-temporal asymmetry of the beat cycle (Herrera-Amaya *et al.* 2021), the amount of thrust produced by a ctene's power stroke is greater than the drag produced by its recovery stroke. Ctenes 'a'–'d' generate a relatively small amount of thrust due to their size, as well as their orientation with respect to the ctenophore's swimming direction. As a result of the ctenophore's body curvature, the orientation of ctenes near the front of the row differs from ctenes further along the row. The effects of ctene orientation on thrust production will be further explored in § 3.4. As shown in figure 10(*b*,*c*), ctenes near the middle of the row ('e'–'l') generate significantly more thrust during their power stroke, as well as more drag during their recovery stroke. Smaller ctenes at the end of the row ('m'–'p', shown in figure 10*d*) also generate only a small amount of thrust with a similar magnitude to the first four ctenes 'a'–'d'. Figure 10(*e*) shows the thrust produced by all sixteen ctenes in the row. This plot demonstrates that due to the phase lag between appendages, a ctene's thrust starts to peak just as an adjacent ctene's thrust begins to decrease. Therefore, throughout the beat cycle, at least one of the ctenes contributes to thrust production, and all sixteen ctenes generate a steady (positive) average thrust (the thick black line in figure 10*e*). This effect may be likened to the functioning of a sixteen-cylinder engine, in which torque is maintained by the sequential firing of the sixteen pistons.

Figure 11 shows a schematic of the vorticity generated by a section of the ctene row at a selected time instant ($t/T = 1.00$). In this figure, ctene 'f' is in the middle of its power stroke and generates a tip vortex (v). Due to the phase lag of metachronal rowing, upstream from this vortex, ctene 'e' generates a smaller vortex (v_u); downstream, recovering ctenes 'g'–'i' produce a shear layer (v_d). These vortices travel through the ctene row together as different ctenes perform their power and recovery strokes. In general, as a ctene enters its power stroke, a positive (red) vortex forms at its tip. This positive vortex contributes to the ctene's thrust generation (Kim & Gharib 2011). Downstream from the positive tip vortex, a negative (blue) shear layer is created as adjacent ctenes perform their recovery stroke. To illustrate the life cycle of the shear layer (v_d), figure 12 identifies two locations along the row where a negative shear layer can be observed. These regions of negative vorticity are labelled $v_{d,1}$ and $v_{d,2}$. At $t/T = 0.25$, $v_{d,1}$ is located near the oral end of the row, and $v_{d,2}$ is located at the aboral end. As the beat cycle progresses, $v_{d,1}$ and $v_{d,2}$ travel through the row, following the propagating metachronal wave as different ctenes perform their

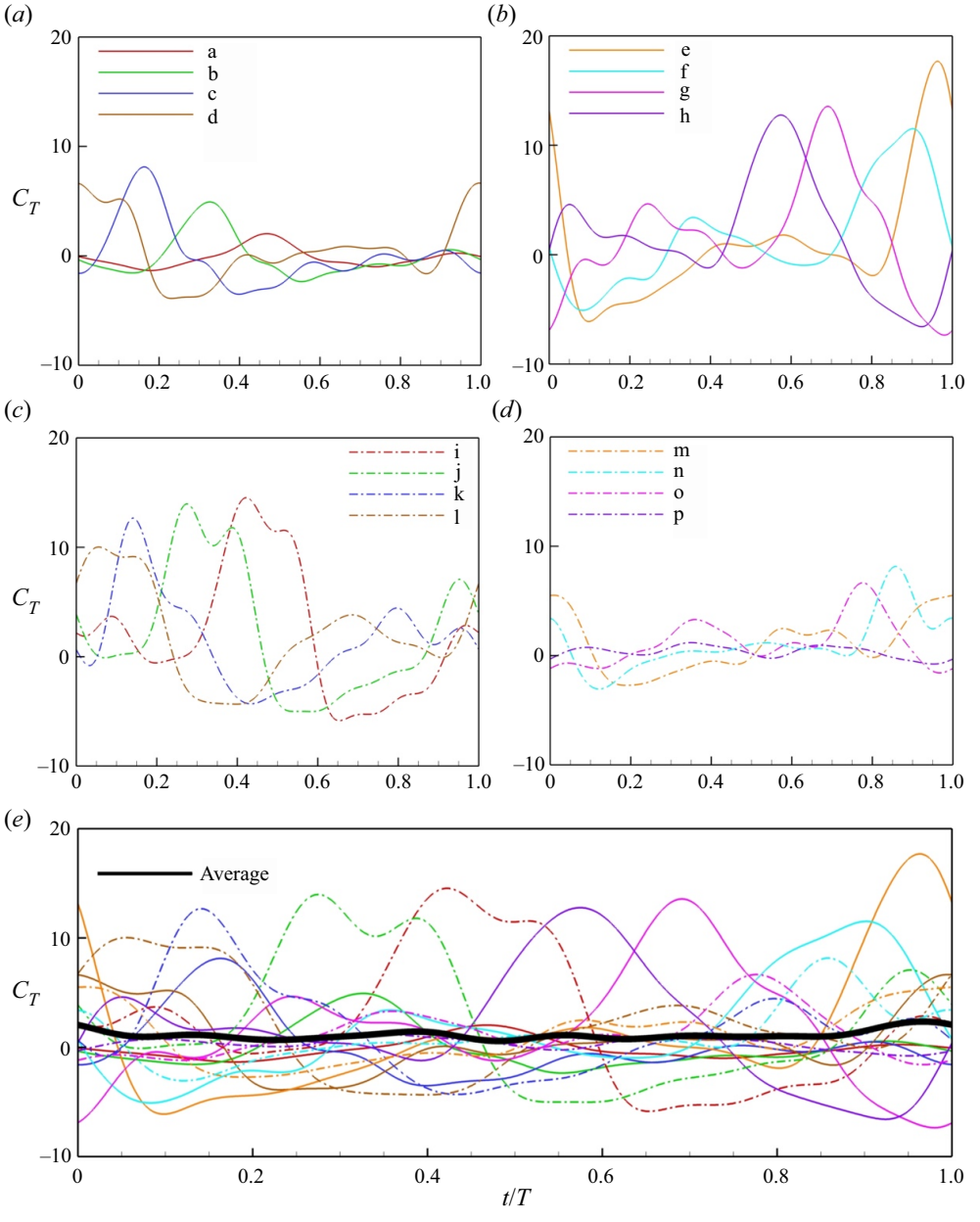

Figure 10. The time-dependent thrust coefficient for the sixteen ctenes throughout one beat cycle. Results are shown for ctenes (*a*) 'a'–'d', (*b*) 'e'–'h', (*c*) 'i'–'l', (*d*) 'm'–'p' and (*e*) all ctenes 'a'–'p'. The thick black line in the last panel (*e*) indicates the averaged thrust over all sixteen ctenes (calculated by summing the thrust produced by all sixteen ctenes, then dividing by the number of ctenes).

recovery strokes. $v_{d,2}$ grows stronger as it nears the middle of the row, while $v_{d,1}$ weakens and disappears as it nears the oral end. At $t/T = 1.00$, $v_{d,2}$ is located approximately where $v_{d,1}$ was located at the start of the beat cycle (further illustrating the periodic nature of metachrony). In this fashion, positive tip vortices and negative shear layers travel through the row along with the metachronal wave. As these tip vortices travel through the ctene

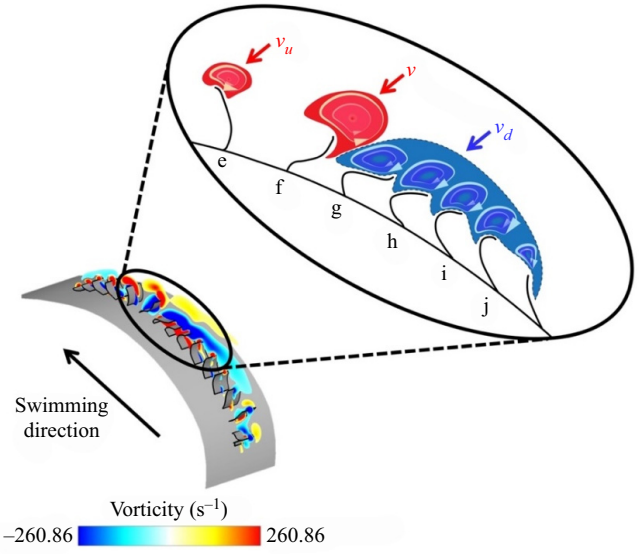

Figure 11. Schematic of the vorticity produced by a portion of the ctene row at $t/T = 1.00$. As ctene 'f' performs its power stroke, it generates a tip vortex, labelled v. Upstream and downstream vortices are labelled v_u and v_d, respectively. The swimming direction of the ctenophore is also labelled; this is also the direction of propagation of the metachronal wave. These results were obtained using the observed natural oscillatory Reynolds number ($Re_\omega = 30$).

row, they undergo complex interactions with corotating and counterrotating neighbouring vortices. In the next section, we determine whether these interactions are constructive or destructive, and we examine how they affect ctene hydrodynamic performance.

3.2. *Vortex interaction mechanism*

Previous studies have suggested that vortex interactions between adjacent metachronal appendages may improve hydrodynamic performance (Ford & Santhanakrishnan 2021*a*,*b*). To determine the mechanism of these interactions, we created a sparse simulation case that features a greater distance between adjacent appendages. This increased distance enabled the observation of ctene hydrodynamics without the effects of vortex interactions. The sparse case was a modification of the original reconstruction and was formed by removing every other ctene along the row. As a result, the sparse case approximately doubles the spacing and phase lag between adjacent appendages. In total, eight ctenes ('b', 'd', 'f', 'h', 'j', 'l', 'n' and 'p') were removed, and original kinematics were preserved for the remaining eight ctenes ('a', 'c', 'e', 'g', 'i', 'k', 'm' and 'o'). The vorticity produced by this sparse case is shown in figure 13. As previously observed, a positive tip vortex is formed as ctenes perform their power stroke. However, due to the increased distance between appendages, recovering ctenes generate distinct negative vortices rather than an attached shear layer.

Figure 14 shows the instantaneous thrust produced by ctenes 'g', 'i' and 'k'. Results are included for the original case and the sparse case. Both cases show that the beat cycle is divided into a thrust-producing power stroke and a drag-producing recovery stroke. However, in the sparse case, ctenes generate slightly more thrust during the power stroke and significantly more drag during the recovery stroke. To explain why this occurs, figure 15 compares the two cases (original vs. sparse) using several snapshots of the

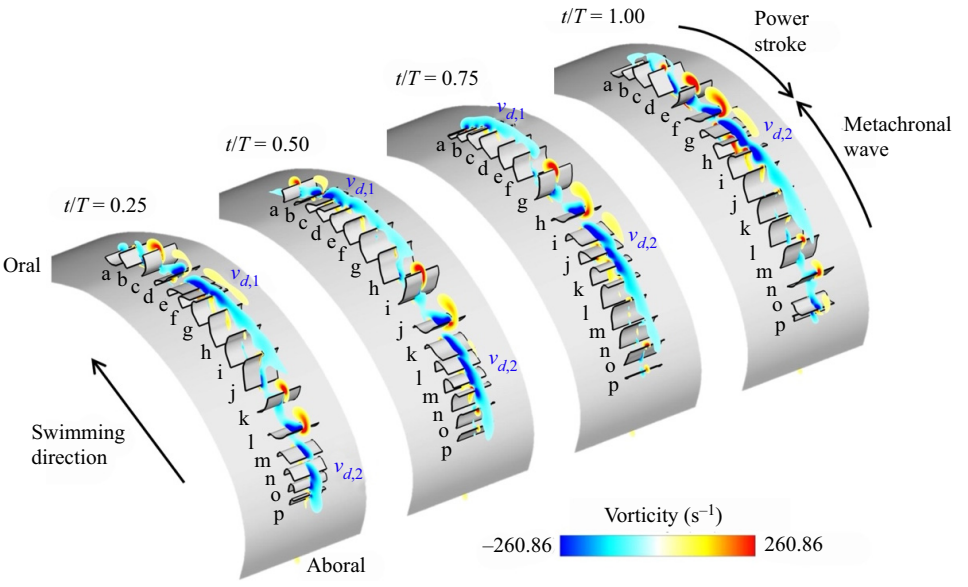

Figure 12. Time sequence of vorticity in the ctene midplane throughout one beat cycle (see supplementary movie available at https://doi.org/10.1017/jfm.2023.739). Negative shear layers are labelled $v_{d,1}$ and $v_{d,2}$, and the sixteen ctenes are labelled alphabetically. The oral and aboral ends of the ctenophore are also labelled. The power stroke direction, metachronal wave direction and swimming direction are shown. These results were obtained using the observed natural oscillatory Reynolds number ($Re_\omega = 30$).

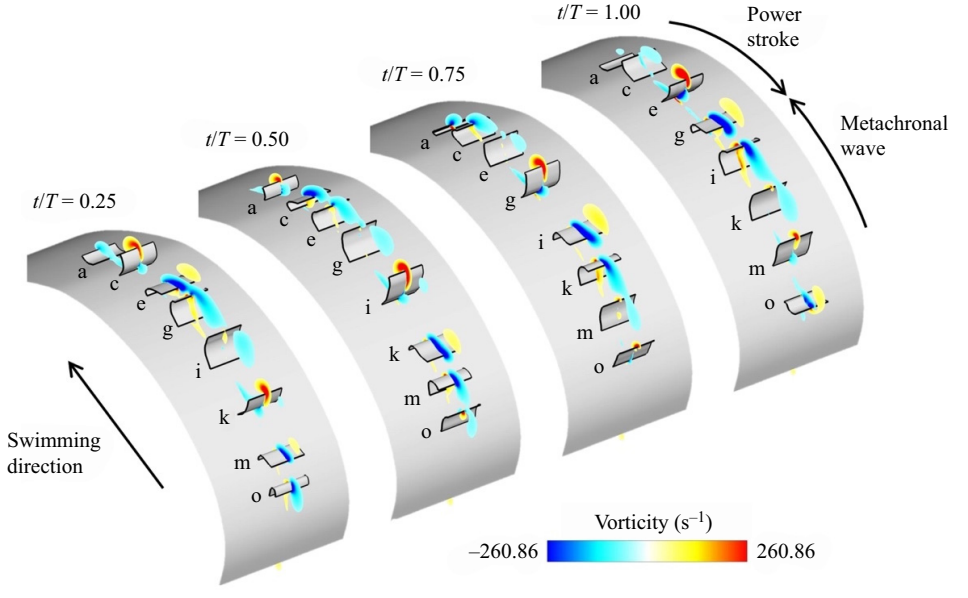

Figure 13. Time sequence of vorticity at the ctene mid-plane generated by the sparse case throughout one beat cycle (see supplemental movie). These results were obtained using the observed natural oscillatory Reynolds number ($Re_\omega = 30$).

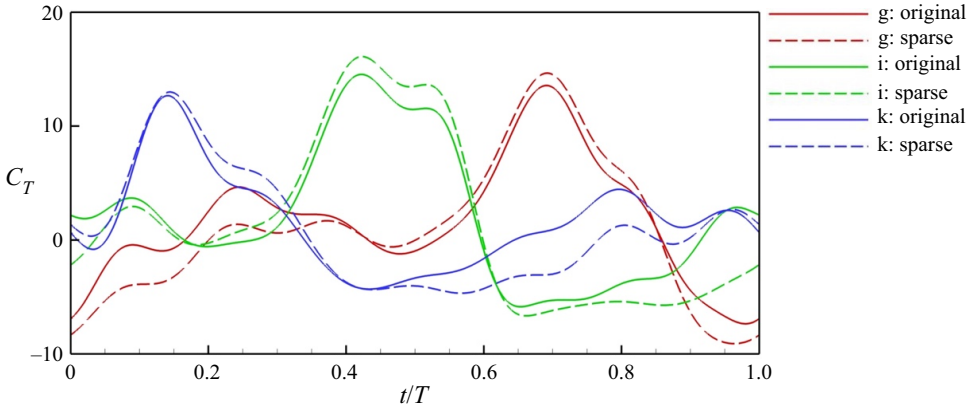

Figure 14. Instantaneous thrust generation by ctenes 'g', 'i' and 'k'. Results are shown for the original case and the sparse case.

vorticity field around ctene 'i'. For both cases, we observe two primary vortices that form during the beating cycle. A positive tip vortex forms during the power stroke (shown for ctene 'i' at $t/T = 0.40$, 0.46 and 0.52). Approximately halfway through the power stroke ($t/T = 0.46$), an additional negative vortex starts to form along the length of the ctene closer to the ctenophore's body. As the ctene transitions from the power stroke to the recovery stroke, the positive tip vortex disappears, and the negative vortex moves along the ctene to become the tip vortex. During the recovery stroke for the original ctene row, the tip vortex attached to ctene 'i' combines with adjacent tip vortices to form a negative shear layer (shown at $t/T = 0.84$, 0.90 and 0.96). For the sparse case, a shear layer does not form during the recovery stroke due to the increased distance between ctenes. Between the end of the recovery stroke and the start of the power stroke, the ctene undergoes a 'rest period' where it is relatively stationary and no obvious tip vortex is present. By comparing the tip vortices shown in figure 15, we observe that the positive power stroke tip vortex attached to ctene 'i' is somewhat smaller in the original case than in the sparse case, which explains why the original case generates slightly less thrust during the power stroke (see figure 14). A similar effect can be observed during the recovery stroke. The section of the recovery shear layer generated by ctene 'i' in the original case is much smaller than the coherent negative vortex generated by ctene 'i' in the sparse case.

Figure 16 more distinctly highlights the difference in tip vortex strength between the original and sparse cases. As tip vortex strength is closely linked to force production (Kim & Gharib 2011), figure 16(*a*) shows the instantaneous total force produced by ctene 'i'. Throughout the beating cycle, the sparse case produces more force than the original case due to greater tip vortex circulation, as shown in figure 16(*b*). To calculate the circulation, we first identified the tip vortices using the λ_2 criterion described by Jeong & Hussain (1995). Compared with other vortex identification methods (e.g. choosing a threshold value of vorticity), the λ_2 criterion is better suited for identifying vortex cores within shear flows, such as the shear layer formed by ctenes during their recovery stroke. Here, λ_2 is defined as the second largest eigenvalue of the tensor $\boldsymbol{S}^2 + \boldsymbol{\Omega}^2$, where $\boldsymbol{S}$ and $\boldsymbol{\Omega}$ are respectively the symmetric and antisymmetric parts of the velocity gradient $\nabla \boldsymbol{V}$. Negative values of λ_2 denote the presence of a vortex. We calculated the circulation Γ using $\Gamma = \int_A \boldsymbol{\omega} \cdot \boldsymbol{n}\, \mathrm{d}A$, where $\boldsymbol{\omega}$ is the vorticity, $\boldsymbol{n}$ is the vector normal to the surface A and A is the area enclosed by a selected contour of λ_2. In this study, we calculated circulation based on $\lambda_2 = -23$. We note that this threshold, while somewhat arbitrary, was chosen because

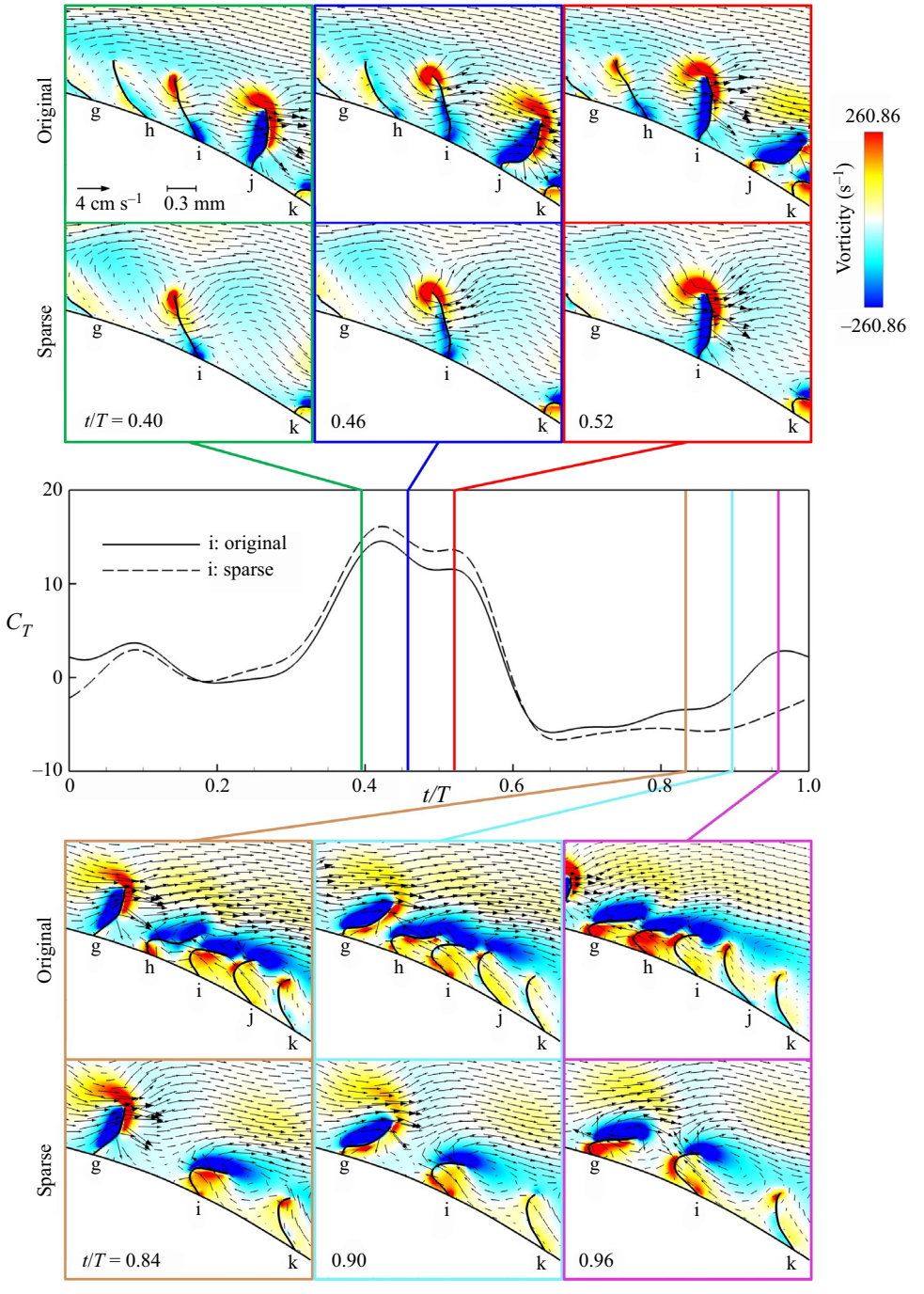

Figure 15. Comparison between the original case and the sparse case. Vorticity and velocity vectors are shown at various instances during the power stroke and recovery stroke of ctene ‘i’.

it clearly distinguishes the power and recovery stroke tip vortices across the beat cycle; a lower magnitude threshold distinguishes the shear layer during the recovery stroke but does not distinguish individual vortices. Using this method, we were able to compare tip vortex circulation between the original and sparse cases. Figure 16(*b*) shows the circulation of the positive and negative vortices attached to ctene 'i' throughout its beat cycle. As described in the previous paragraph, the negative vortex that will become the recovery stroke tip vortex begins to form during the power stroke; this explains the overlap between positive and negative circulation shown in figure 16(*b*). This plot demonstrates that vortex circulation is always weaker in the original ctene row between $t/T = 0.35$ and 0.92 (comprising 57 % of the total beating cycle). It is worth noting that approximately 82 % of total force production occurs during this period, which demonstrates the importance of vortex-weakening mechanism on the overall force generation. The difference in tip vortex strength can also be observed in figure 16(*c*,*d*), which show the vorticity around ctene 'i' for the original and sparse cases, respectively. In these images, positive and negative vortices are labelled with '$+\Gamma$' and '$-\Gamma$', and contours are shown for $\lambda_2 = -23$. At both time instances shown, the tip vortex is visibly smaller in the original ctene row. These results further demonstrate that tip vortices are weaker in the original row, resulting in reduced force production.

Because tip vortices are consistently weaker in the original case, we propose that ctenophores employ a vortex-weakening mechanism to enhance their hydrodynamic performance. Through this mechanism, ctene tip vortices (both positive and negative) are weakened by destructive interactions with neighbouring vortices. In metachronal rowing, the distance between ctene tips increases during the power stroke, and ctene tips are brought closer together during the recovery stroke. As a result, destructive tip vortex interactions are minimized during the thrust-producing power stroke and maximized during the drag-producing recovery stroke. This has the overall effect of increasing the average thrust produced by the ctenes, as shown in figure 17.

In figure 17, the cycle-averaged force generation (both lift and thrust), power consumption and thrust-to-power ratio (C_T/C_{PW}) for each ctene are compared between the original case and the sparse case. As shown in figure 17(*a*), ctenes in the original case generate more thrust, which can be attributed to the proposed vortex-weakening mechanism. This mechanism significantly reduces drag generation during the recovery stroke, which outweighs the slight decrease in thrust during the power stroke. As a result, overall thrust generation is improved (as shown via higher cycle-averaged C_T). Figure 17(*a*) also shows that the larger ctenes near the middle of the row produce the most cycle-averaged thrust and show the largest difference in C_T between the original and sparse cases.

Figure 17(*b*) presents the force component generated in the vertical (y) direction (lift coefficient, C_L), averaged over the beat cycle. Both original and sparse cases follow a similar trend across ctenes, with similar magnitudes of lift generated for both cases. Figure 17(*c*) displays the average power consumed by each ctene. This plot shows that ctenes in the original case consume less power, which is another benefit of the vortex-weakening mechanism. This mechanism reduces the magnitude of instantaneous thrust production throughout the beat cycle, and as a result, ctenes consume less power. Figure 17(*d*) shows that the average ctene thrust-to-power ratio is higher for ctenes in the original case than ctenes in the sparse case. In both cases, the first few ctenes in the row have the lowest thrust-to-power ratio, and the last few ctenes have the greatest thrust-to-power ratio. Table 4 reports the averaged thrust generation, power consumption and thrust-to-power ratio for the entire ctene row. To make a fair comparison, these values

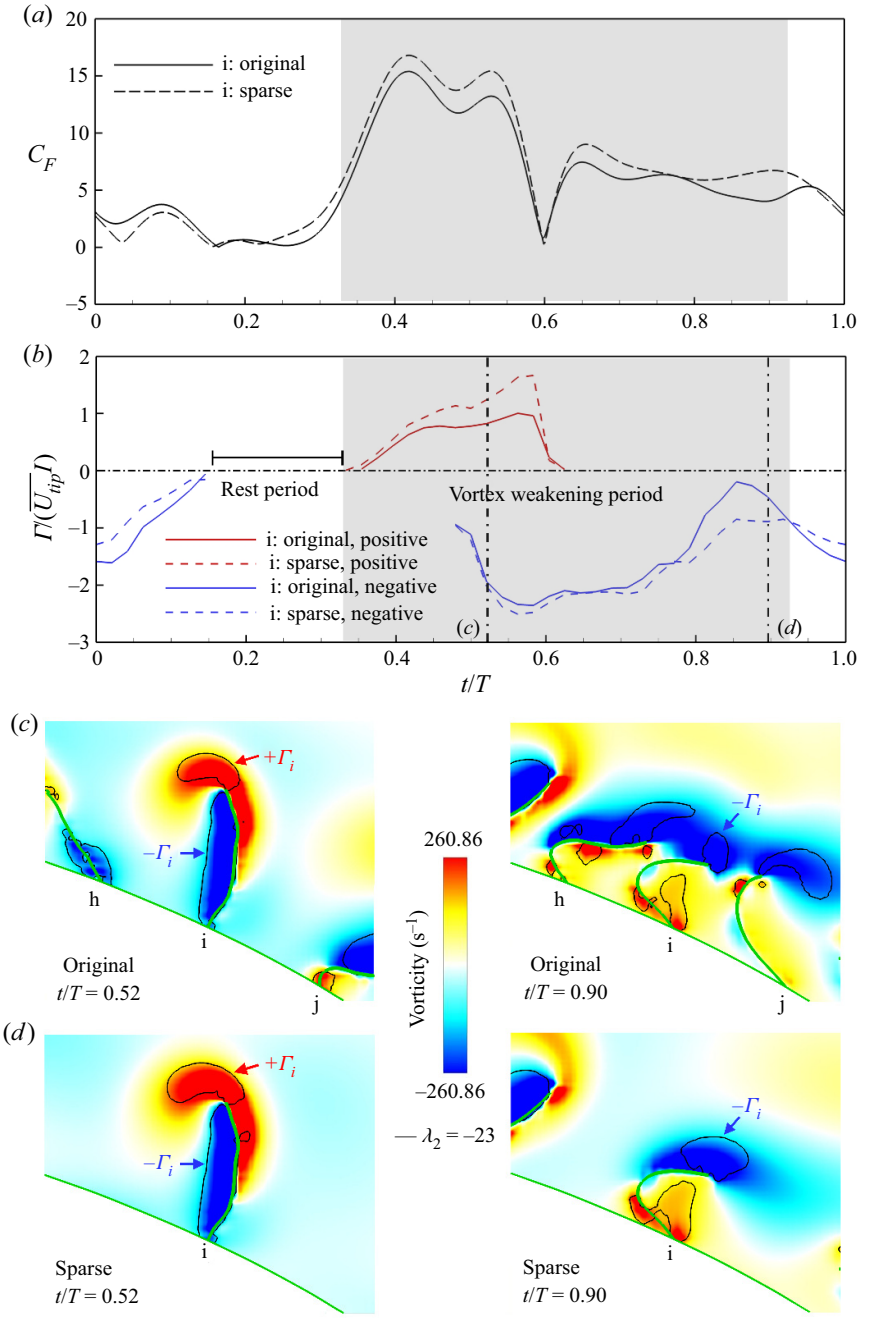

Figure 16. (*a*) The instantaneous total force produced by ctene 'i'. (*b*) The normalized circulation of the tip vortex attached to ctene 'i', calculated using $\lambda_2 = -23$. The vortex-weakening period is shaded in grey. (*c*,*d*) Show the vorticity around ctene 'i' for the original and sparse cases, respectively. The tip vortex is shown during the power stroke ($t/T = 0.52$) and the recovery stroke ($t/T = 0.90$). Positive and negative vortices are labelled with '$+\Gamma$' and '$-\Gamma$', and contours are shown for $\lambda_2 = -23$.

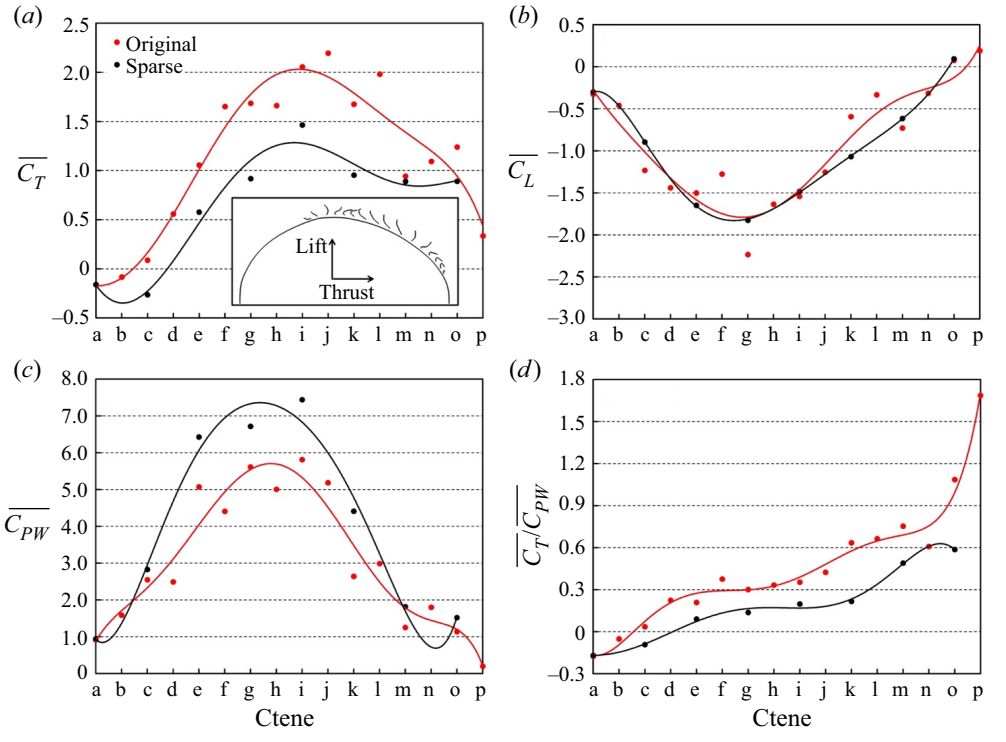

Figure 17. Cycle-averaged (*a*) thrust generation, (*b*) lift generation, (*c*) power consumption and (*d*) thrust-to-power ratio for each ctene along the row. Results are shown for the original case and the sparse case. In each plot, the data were fitted using a six-term polynomial trendline. The direction of thrust and lift relative to the ctene row is shown in the inset of (*a*).

	$\overline{C_T}$	$\overline{C_{PW}}$	$\overline{C_T}/\overline{C_{PW}}$
Original case	1.07	3.13	0.40
Sparse case	0.66 (↓ 38.32 %)	4.01 (↑ 28.12 %)	0.18 (↓ 55.00 %)

Table 4. Average ctene row performance for the original case and the sparse case (calculated by averaging over all ctenes in the row). For a fair comparison, only eight ctenes of the original case ('a', 'c', 'e', 'g', 'i', 'k', 'm' and 'o') are counted for the calculation.

were calculated by averaging the performance of the eight ctenes within the row ('a', 'c', 'e', 'g', 'i', 'k', 'm' and 'o') simulated in both the original and sparse cases. Compared with the original row, the sparse row generates 38.32 % less thrust, consumes 28.12 % more power and has a 55.00 % lower thrust-to-power ratio.

These results indicate that the newly proposed vortex-weakening mechanism significantly improves the hydrodynamic performance of metachronal rowing. This mechanism also provides some insight into the evolution of metachronal rowing in ctenophores and other species. In a row of beating appendages, there is evolutionary pressure to increase the distance between appendages, so that thrust-enhancing tip vortices

can form during the power stroke. However, there is also pressure to decrease the distance between appendages, so that drag-producing tip vortices formed during the recovery stroke can be weakened by moving appendage tips closer together. It is therefore likely that there exists an optimal combination of appendage spacing and spatio-temporal kinematics that maximizes the performance-enhancing effects of the vortex-weakening mechanism. In ctenophores, the flexibility of the appendage allows for closer spacing during the recovery stroke vs. the power stroke; the material properties and bending dynamics of ctenes may therefore have been influenced over evolutionary time by this fluid mechanical constraint on performance. Furthermore, the optimal spacing is likely to be Reynolds number dependent, as explored in the next section.

Several previous studies have examined how appendage spacing and kinematics affect hydrodynamic performance, but have not examined the underlying flow mechanisms in detail. Dauptain *et al.* (2008) found that ctenophore swimming is most efficient when the ratio of appendage spacing to appendage length is close to 0.5. This optimal spacing is likely a consequence of the vortex-weakening mechanism. As described in the previous paragraph, the distance between appendages must be large enough to allow the formation of strong tip vortices during the power stroke, but small enough to weaken tip vortices formed during the recovery stroke. Other studies have shown that metachronal rowing results in a greater average body speed than synchronous rowing, in which the phase lag is zero (Alben *et al.* 2010; Ford & Santhanakrishnan 2021*b*). Our results indicate that a primary benefit of the phase lag, in combination with the time-varying shape of the beating ctene, is to increase the distance between ctene tips during the power stroke and reduce the distance between ctene tips during the recovery stroke. As a result, destructive tip vortex interactions are minimized during the thrust-producing power stroke and maximized during the drag-producing recovery stroke. These findings suggest that the vortex-weakening mechanism is a combined effect of multiple morphological (e.g. appendage spacing) and kinematic (e.g. phase lag and bending) parameters involved in metachronal rowing.

The identification of the vortex-weakening mechanism enhances our understanding of the hydrodynamic principles underlying metachronal rowing. For example, Colin *et al.* (2020) found that metachronal swimmers generate thrust by creating negative pressure fields along the leeward side of their appendages. In ctenophores, this ‘suction thrust’ is a result of the bending kinematics of the beating ctenes. Our findings suggest that ctene bending also promotes destructive tip vortex interactions between neighbouring appendages during the recovery stroke, which significantly improve the ctenophore’s overall thrust production. The vortex-weakening mechanism can also be compared with appendage interaction mechanisms that occur across different flow regimes. In Stokes flow conditions ($Re \ll 1$), recent studies have identified a ciliary ‘shielding effect’ in which the flow generated by a beating cilium is obstructed by adjacent cilia (Khaderi, Den Toonder & Onck 2011; Milana *et al.* 2020; Zhang, den Toonder & Onck 2021, 2022). This effect is present throughout the entire beating cycle, but it is especially pronounced during the recovery stroke, leading to an overall increase in net flow. This shielding effect functions similarly to the vortex-weakening mechanism, as some performance is sacrificed during the power stroke to enable significant performance gains during the recovery stroke (see figure 14). However, cilia typically beat with a much lower Reynolds number ($Re \ll 1$) than the ctenes observed in this study ($Re_\omega = 30$). In the next section, we will explore how the vortex-weakening mechanism is affected by artificially increasing and decreasing Re.

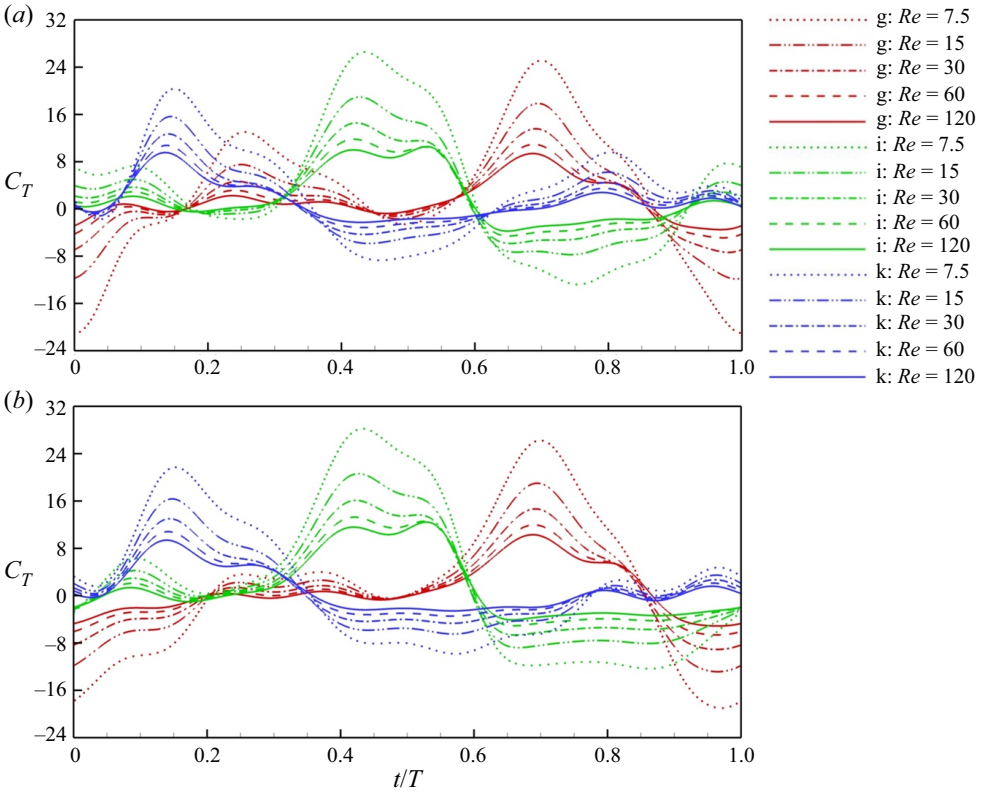

Figure 18. Instantaneous thrust generation by ctenes 'g', 'i' and 'k' at different Reynolds numbers ($Re_\omega = 7.5$, $Re_\omega = 15$, $Re_\omega = 30$, $Re_\omega = 60$, $Re_\omega = 120$). Results are shown for (*a*) the original ctene row and (*b*) the sparse row.

3.3. *Effects of varying the Reynolds number*

In this section, we aim to examine how ctenophores' propulsion mechanism changes as the Reynolds number varies between 7.5 and 120. Across this range of Re_ω, we ran simulations using both the original ctene row and the sparse row. Figure 18(*a*) shows the thrust produced by ctenes 'g', 'i' and 'k' in the original row. As Re_ω increases, less (non-dimensional) thrust is generated during the power stroke, and less drag is generated during the recovery stroke. In other words, the instantaneous magnitudes of the horizontal force coefficients are reduced throughout the beat cycle. Figure 18(*b*) displays similar results for the sparse row.

To explain this trend, figure 19 shows how varying Re_ω affects the vortex structures produced by the ctene row. At lower Reynolds numbers, ctenes generate attached tip vortices and shear layers. However, as Re_ω increases, these vortices start to detach from the ctene tips. In the observed natural ctenophore swimming ($Re_\omega = 30$), attached tip vortices and shear layers enhance ctene force production (Kim & Gharib 2011). Therefore, vortex detachment at higher Re_ω reduces the magnitude of force generation throughout the beat cycle, as shown in figure 18. These observations suggest that the vortex-weakening mechanism is more effective at improving thrust performance in the low-to-intermediate Reynolds number regime, in which tip vortices and shear layers remain attached to the beating ctenes.

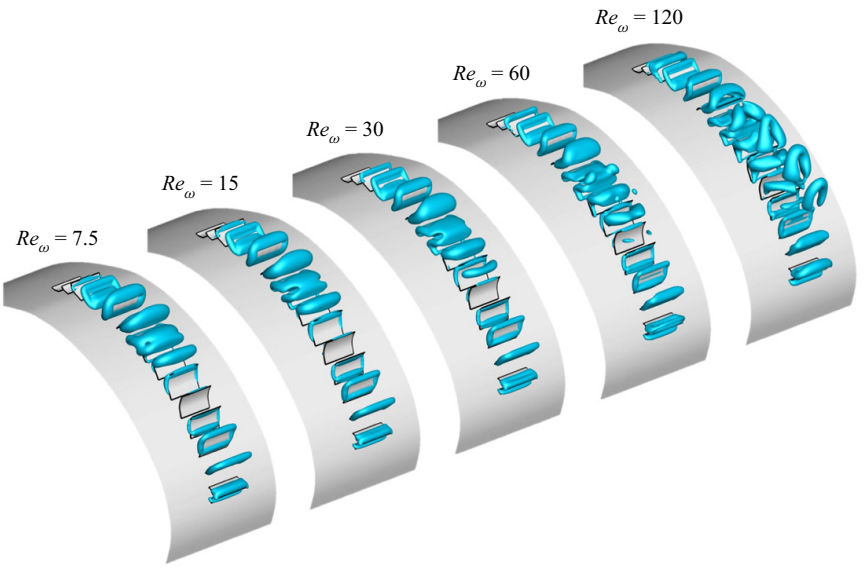

Figure 19. The Q-isosurface vortex structures generated by the original ctene row at $t/T = 1.00$. Results are shown for $Re_\omega = 7.5$, $Re_\omega = 15$, $Re_\omega = 30$, $Re_\omega = 60$ and $Re_\omega = 120$. See movie in the supplementary material.

Figure 20 shows how Re_ω affects the cycle-averaged ctene performance. For ctenes in the original row, average thrust production and power consumption decrease as Re_ω becomes larger. The decrease in thrust generation is caused by the detachment of tip vortices and shear layers, and the decrease in power consumption is a result of the thinner boundary layer at higher Re_ω. The ctene thrust-to-power ratio (C_T/C_{PW}) improves as Re_ω becomes larger. The sparse ctene row exhibits similar trends in power consumption and thrust-to-power ratio. However, unlike the original row, increasing Re_ω does not impact overall thrust production as dramatically, as shown in table 5. This difference is a result of the proposed vortex-weakening mechanism, which does not play a role in the sparse row.

In the original row, attached tip vortices interact to reduce the amount of drag produced by recovering ctenes. When tip vortices detach at higher Re_ω, this drag-reducing effect is lost and ctenes therefore generate less average thrust. The sparse ctene row does not benefit from tip vortex interactions very much, and as a result, its average thrust generation is significantly less sensitive to varying Re_ω. These trends are summarized in table 5, which shows the average ctene row performance for each case. As Re_ω increases, the original row produces less (non-dimensional) thrust, consumes less power, and its thrust-to-power ratio increases. The sparse row exhibits similar trends in power consumption and thrust-to-power ratio. However, for reasons described above, its thrust generation is less affected by changing Re_ω. Interestingly, when considering swimming ctenophores, animals (such as *Beroe* sp.) which beat their ctenes at higher frequencies (and correspondingly higher Re_ω) also have closer ctene spacing, indicating that the vortex-weakening mechanism may extend to higher Re_ω if the spacing between ctenes is decreased.

3.4. *Effects of varying substrate curvature*

To determine how body curvature affects ctene hydrodynamics, we progressively flattened the model substrate used in this study (for details, see Appendix E). We ran simulations

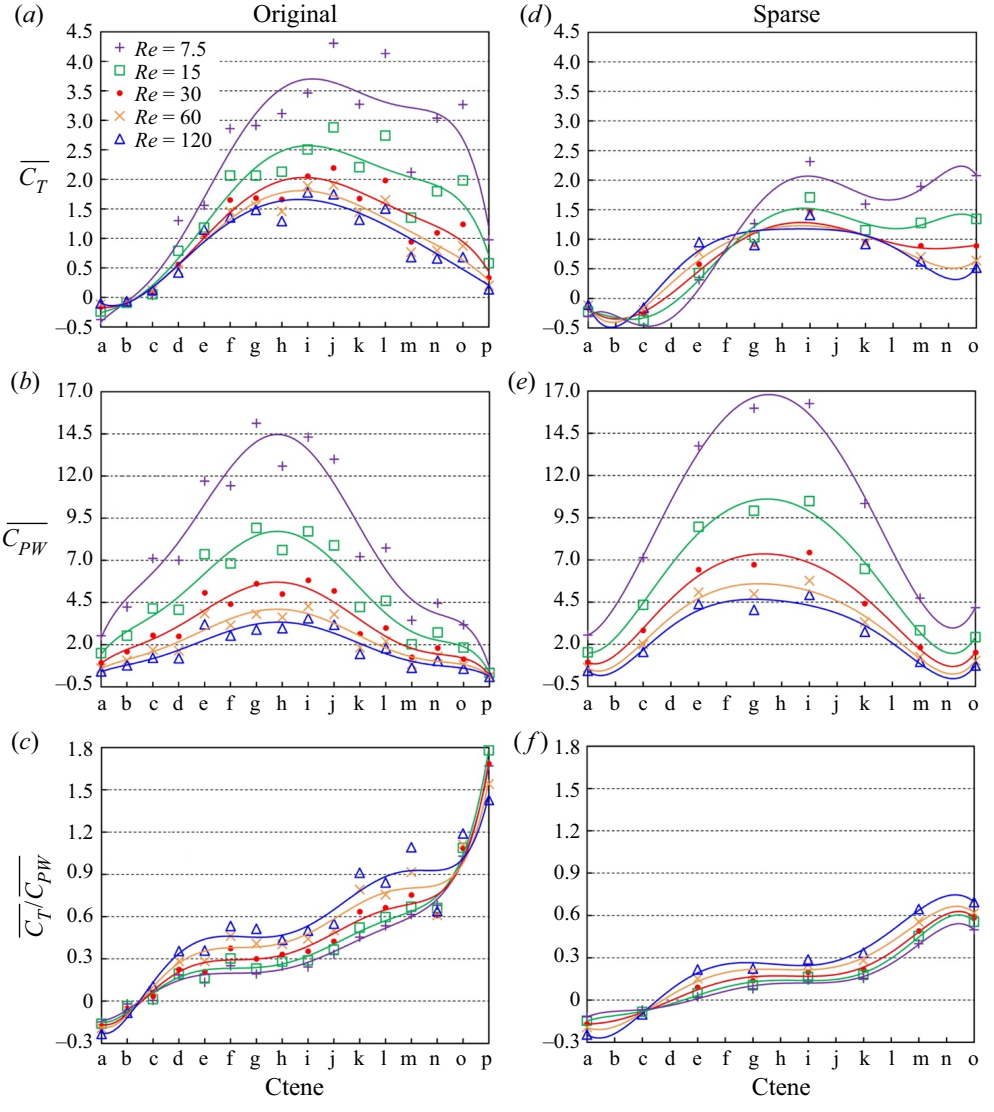

Figure 20. Cycle-averaged thrust, power and thrust-to-power ratio for each ctene. Results are shown for $Re_\omega = 7.5$, $Re_\omega = 15$, $Re_\omega = 30$, $Re_\omega = 60$ and $Re_\omega = 120$. The left column (*a–c*) includes results for the original ctene row, and the right column (*d–f*) includes results for the sparse row.

using four different substrate curvatures, including the original curvature, medium curvature, low curvature and flat. For each substrate geometry, simulations were run using both the original ctene row and the sparse row (using the original ctene kinematics and Reynolds number). Figure 21 shows the vorticity produced by the original row along each of the different substrate curvatures. As previously observed, ctenes generate a positive vortex during their power stroke, and they generate a negative shear layer during their recovery stroke. These vortex formations are consistent across all four substrate curvatures. Figure 22 displays similar results for the sparse ctene row.

Figure 23 shows the cycle-averaged ctene performance for each substrate curvature. Figure 23(*a*) includes the average thrust produced by ctenes in the original row. For the

		$\overline{C_T}$	$\overline{C_{PW}}$	$\overline{C_T}/\overline{C_{PW}}$
Original row	$Re_\omega = 7.5$	2.24 (↑ 100 %)	7.85 (↑ 158.22 %)	0.40 (↓ 14.89 %)
	$Re_\omega = 15$	1.50 (↑ 33.93 %)	4.70 (↑ 54.61 %)	0.43 (↓ 8.51 %)
	$Re_\omega = 30$	1.12	3.04	0.47
	$Re_\omega = 60$	0.97 (↓ 13.39 %)	2.16 (↓ 28.95 %)	0.52 (↑ 10.44 %)
	$Re_\omega = 120$	0.89 (↓ 20.54 %)	1.72 (↓ 43.42 %)	0.57 (↑ 21.28 %)
Sparse row	$Re_\omega = 7.5$	1.08 (↑ 63.64 %)	9.37 (↑ 133.67 %)	0.14 (↓ 22.22 %)
	$Re_\omega = 15$	0.79 (↑ 19.70 %)	5.87 (↑ 46.38 %)	0.16 (↓ 11.11 %)
	$Re_\omega = 30$	0.66	4.01	0.18
	$Re_\omega = 60$	0.63 (↓ 4.55 %)	3.01 (↓ 27.18 %)	0.22 (↑ 22.22 %)
	$Re_\omega = 120$	0.63 (↓ 4.55 %)	2.48 (↓ 38.15 %)	0.26 (↑ 44.44 %)

Table 5. Average ctene row performance for different values of Re_ω. Results are presented for the original ctene row and the sparse row.

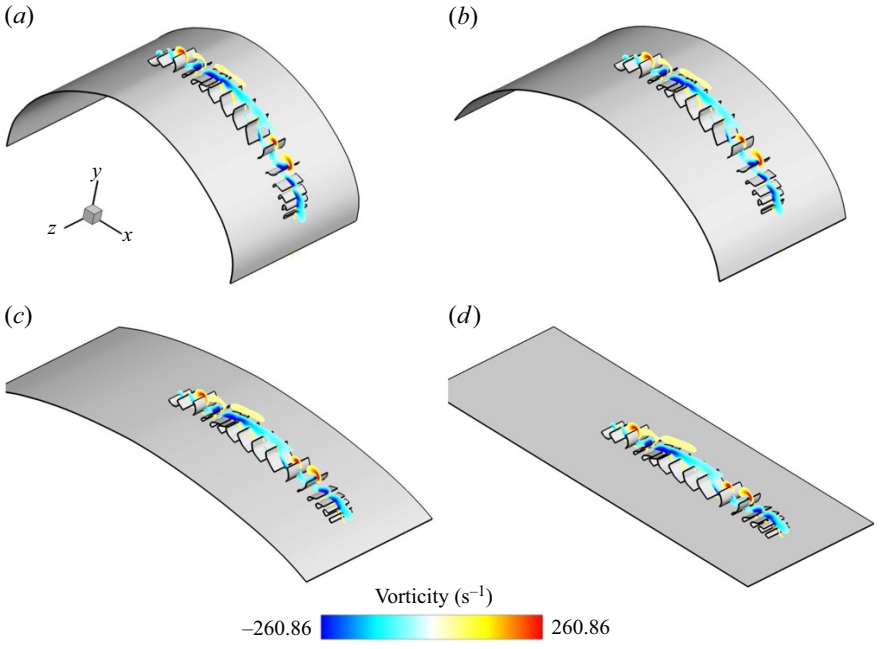

Figure 21. Vorticity generated by the original ctene row at $t/T = 0.25$. Results are shown for different substrate curvatures, including (*a*) the original curvature, (*b*) medium curvature, (*c*) low curvature and (*d*) flat.

first four ctenes ('a'–'d'), the original curvature generates less thrust than the other three curvatures. However, for the remaining twelve ctenes ('e'–'p'), the original curvature generates significantly more thrust. Figure 23(*b*) shows the average lift produced by ctenes in the original row. For the first five ctenes ('a'–'e'), all curvatures generate approximately the same amount of lift. However, for the other eleven ctenes ('f'–'p'), the original curvature produces less lift than the other curvatures. Average total force generation, shown in figure 23(*c*), remains relatively unchanged by substrate curvature.

Similar trends are observed for the sparse row, as seen in figure 23(*d–f*). In addition, figure 24 shows that as the substrate flattens, ctene power consumption remains unchanged (and, therefore, the thrust-to-power ratio decreases). These results are summarized in

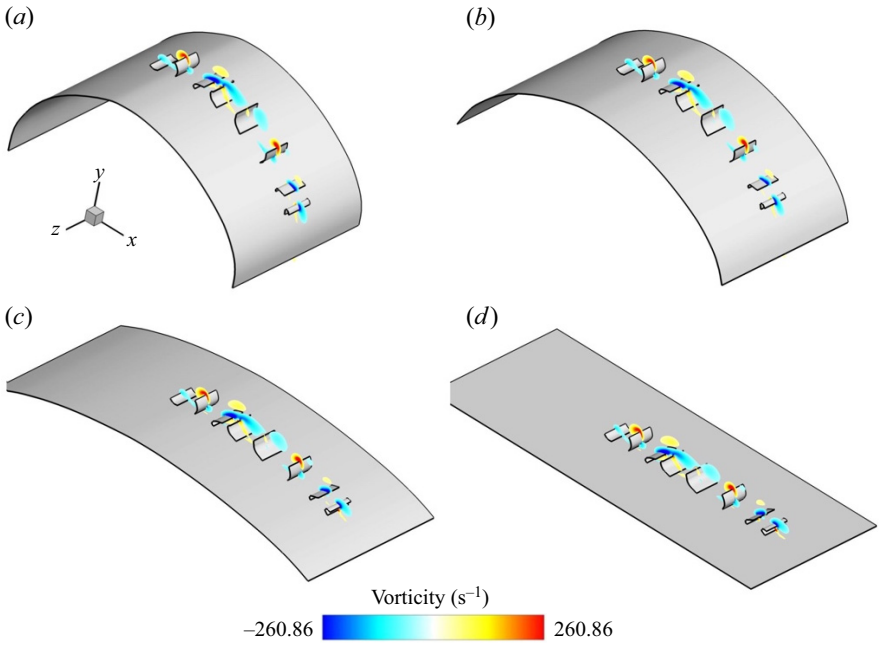

Figure 22. Vorticity generated by the sparse ctene row at $t/T = 0.25$. Results are shown for different substrate curvatures, including (*a*) the original curvature, (*b*) medium curvature, (*c*) low curvature and (*d*) flat.

tables 6 and 7. Table 6 shows that as the substrate flattens, the ctene row overall generates less thrust and more lift, while its total force production is relatively unaffected. Table 7 shows that the ctene row consumes the same amount of power as it flattens, while its thrust-to-power ratio decreases. Since total force production is related to tip vortex strength, it is likely that that tip vortex circulation is also relatively unaffected by substrate curvature. This is demonstrated in figure 25, which shows the circulation of the tip vortex attached to ctene 'i'. Between the original substrate curvature and the flat substrate, we do not observe any significant differences in tip vortex circulation. We also determined that for the original substrate curvature, vortex interactions weaken the tip vortex by a maximum of 42 % during the power stroke and 77 % during the recovery stroke. For the flat curvature, the tip vortex is weakened by a maximum of 39 % during the power stroke and 85 % during the recovery stroke. This suggests that the proposed vortex-weakening mechanism is active regardless of substrate curvature and is effective across a variety of body morphologies. We can therefore infer that the vortex-weakening mechanism is present in most instances of metachronal rowing in the low-to-intermediate Reynolds number regime, including ciliary flows (Elgeti & Gompper 2013; Granzier-Nakajima *et al.* 2020), paramecia swimming (Zhang *et al.* 2015) and ctenophore swimming among different species (Tamm 2014; Gibbons *et al.* 2021).

As previously mentioned, total ctene force production, power consumption and tip vortex circulation are not significantly affected by substrate curvature. This indicates that the performance benefits (as measured by higher C_T) of a curved substrate are not a result of vortex interactions or other unsteady flow features. We therefore hypothesize that, in our simulations, varying the substrate curvature (while preserving the original kinematics) affects ctenophore hydrodynamic performance simply by reorienting the direction of ctene motion. To illustrate the effects of ctene orientation, figure 26 depicts the thrust and lift vectors produced by ctene 'k' as it experiences maximum force production.

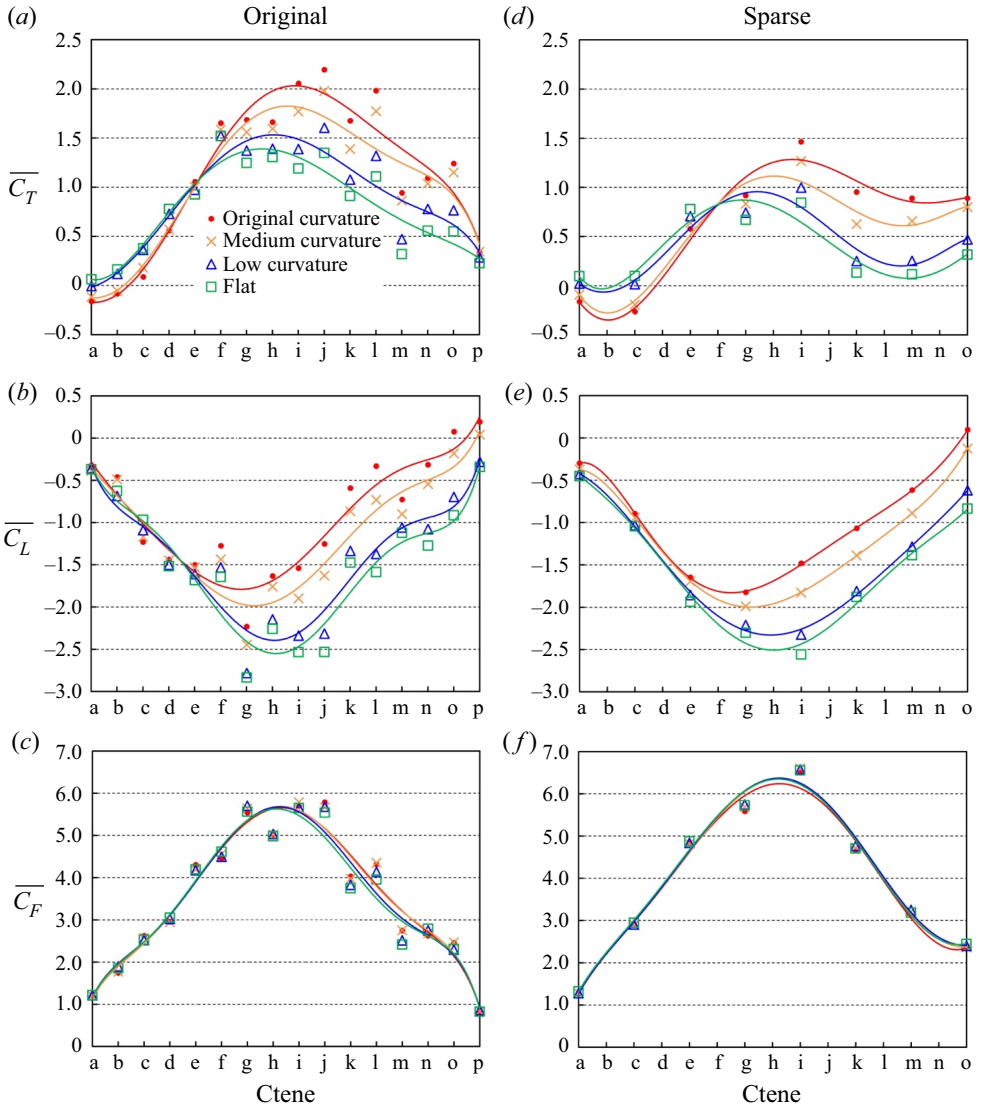

Figure 23. Cycle-averaged ctene force generation (thrust, lift and overall force coefficients) for each substrate curvature. Results are shown for the original ctene row (*a–c*) and the sparse row (*d–f*).

Figure 26(*a*) shows that in the original substrate curvature, ctene 'k' is oriented perpendicular to the ctenophore's swimming direction. In this orientation, it generates mostly thrust and almost no lift. Figure 26(*b*) shows that in the flat substrate curvature, ctene 'k' is more parallel to the ctenophore's swimming direction. In this orientation, it produces less thrust and more lift. Based on these observations, we conclude that most of the ctenes along the original substrate are oriented so that during the peak of their power stroke, they are roughly perpendicular to the ctenophore's direction of motion. As a result, these ctenes displace fluid directly behind the ctenophore's body, which maximizes their thrust generation. In contrast, ctenes along the reconstructed flat substrate experience their maximum force production while oriented more parallel to the ctenophore's direction of motion. Therefore, ctenes along the flat substrate generate less thrust and more lift.

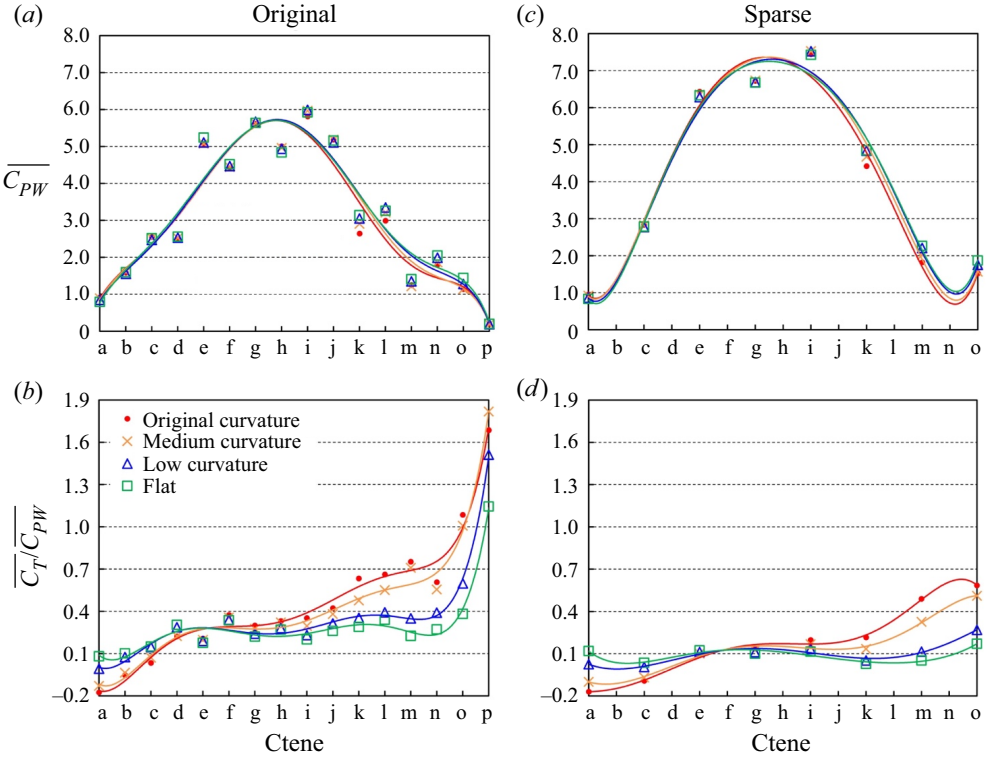

Figure 24. Cycle-averaged ctene power consumption and thrust-to-power ratio for each substrate curvature. Results are shown for the original ctene row (*a*,*b*) and the sparse row (*c*,*d*).

		$\overline{C_T}$	$\overline{C_L}$	$\overline{C_F}$
Original row	Original curvature	1.12	−0.91	3.52
	Medium curvature	1.04 (↓ 7.14 %)	−1.09 (↑ 19.78 %)	3.52 (− 0.00 %)
	Low curvature	0.88 (↓ 21.43 %)	−1.39 (↑ 52.75 %)	3.48 (↓ 1.14 %)
	Flat	0.79 (↓ 29.46 %)	−1.48 (↑ 62.64 %)	3.45 (↓ 1.99 %)
Sparse row	Original curvature	0.66	−0.97	3.91
	Medium curvature	0.57 (↓ 13.64 %)	−1.15 (↑ 18.56 %)	3.95 (↑ 1.02 %)
	Low curvature	0.43 (↓ 34.85 %)	−1.45 (↑ 49.48 %)	3.97 (↑ 1.53 %)
	Flat	0.38 (↓ 42.42 %)	−1.55 (↑ 59.79 %)	3.97 (↑ 1.53 %)

Table 6. Average ctene row force generation for different substrate curvatures. Results are presented for the original ctene row and the sparse row.

The same trend is observed for most of the ctenes in the row. This is demonstrated in figure 27, which shows the average thrust and lift vectors for each ctene along the different substrate curvatures. As the substrate curvature flattens, ctenes on average generate less thrust and more lift. However, in real ctenophore forward swimming, lift does not contribute to propulsion due to radial symmetry (as illustrated in the subplot of figure 27*a*). Due to the symmetrical arrangement of ctene rows around the ctenophore's body, lift generated by one row is negated by the row located directly across the body. Because the original substrate curvature generates the least lift and most thrust, it provides

		$\overline{C_{PW}}$	$\overline{C_T}/\overline{C_{PW}}$
Original row	Original curvature	3.04	0.46
	Medium curvature	3.08 (↑ 1.32 %)	0.44 (↓ 4.35 %)
	Low curvature	3.12 (↑ 2.63 %)	0.36 (↓ 21.74 %)
	Flat	3.14 (↑ 3.29 %)	0.30 (↓ 34.78 %)
Sparse row	Original curvature	4.01	0.18
	Medium curvature	4.07 (↑ 1.50 %)	0.15 (↓ 16.67 %)
	Low curvature	4.11 (↑ 2.49 %)	0.10 (↓ 44.44 %)
	Flat	4.12 (↑ 2.74 %)	0.092 (↓ 48.89 %)

Table 7. Average ctene row power consumption and thrust-to-power ratio for different substrate curvatures. Results are presented for the original ctene row and the sparse row.

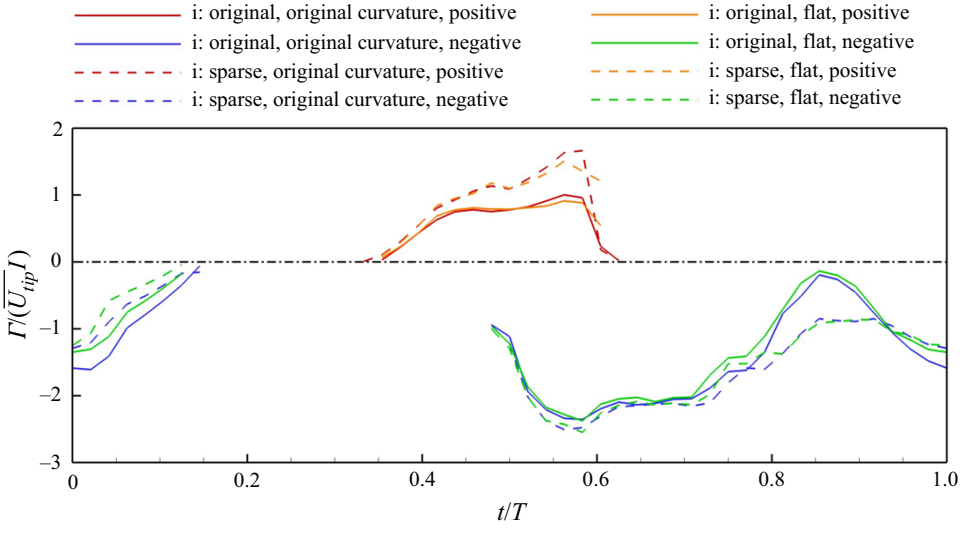

Figure 25. Effects of substrate curvature on the circulation of the tip vortex attached to ctene 'i'. Results are shown for the original substrate curvature and the flat substrate using the original ctene row and the sparse row.

the best hydrodynamic performance of the four curvatures tested. However, this is because we preserved the original ctene kinematics while rotating them into a flat configuration (see Appendix E). Real ctenophores have a high degree of variability in body curvature, and it is likely that the ctene kinematics are tuned to accommodate this variability; this may be accomplished by altering the position of the stroke amplitude 'cone' shown in figure 4 and/or the shape of the power and recovery strokes to ensure that force production is maximized in the swimming direction. Future investigations of living animals may wish to focus on how ctenes are oriented with respect to the body wall throughout the beat cycle, and how this varies with body curvature.

Another interesting effect of body curvature is that for the first few ctenes in the row ('a'–'d'), the flat substrate produces the most thrust and displays the highest thrust-to-power ratio. In fact, ctenes 'a' and 'b' along the original curvature even generate a small amount of drag, as shown in figure 23(*a*). For ctenes further along the row ('e'–'p'), this trend reverses, and the original curvature provides far superior performance. Figures 26 and 27 help illustrate why this shift occurs. In the original curvature, the

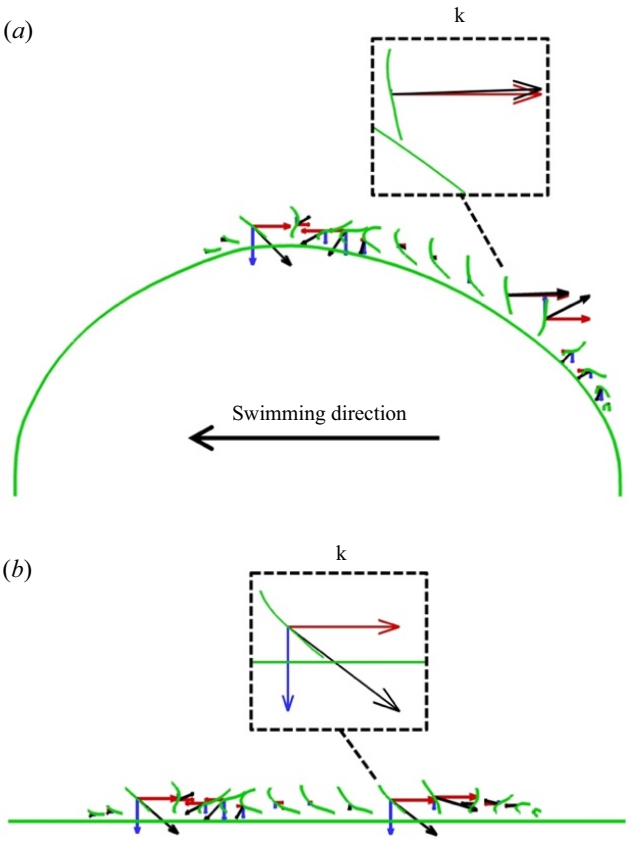

Figure 26. Vector diagram showing the thrust (coloured red) and lift (coloured blue) produced by each ctene at $t/T = 0.15$. At this particular time instant, ctene 'k' (shown in subplot) is experiencing maximum force production. Results are compared between (*a*) the original and (*b*) flat substrate curvatures.

first few ctenes are angled slightly toward the front of the ctenophore's body, leading to diminished thrust and, for ctenes 'a' and 'b', slight drag. Further along the row, ctenes are angled behind the ctenophore's body, which is a more optimal configuration for thrust production. This is a primary reason why, in nature, ctenes are located mainly along the back half of the ctenophore's body. However, ctenophores are capable of a wide variety of swimming manoeuvres, including near-omnidirectional swimming and turning (Herrera-Amaya & Byron 2023). This could account for the presence of ctenes 'a' and 'b'; although they slightly degrade the ctenophore's thrust generation, they likely contribute to performance in other modes of swimming.

4. Conclusions

In this study, we simulated ctenophore swimming kinematics using an in-house immersed-boundary-method-based CFD solver. Our simulation results show that ctenes form a thrust-producing tip vortex during their power stroke and a drag-producing shear layer during their recovery stroke. As ctenes beat metachronally, these vortices interact to enhance hydrodynamic performance. We propose that this enhancement occurs via destructive interactions between neighbouring tip vortices. Ctene tips move apart during their power stroke and move toward each other during their recovery stroke. As a result,

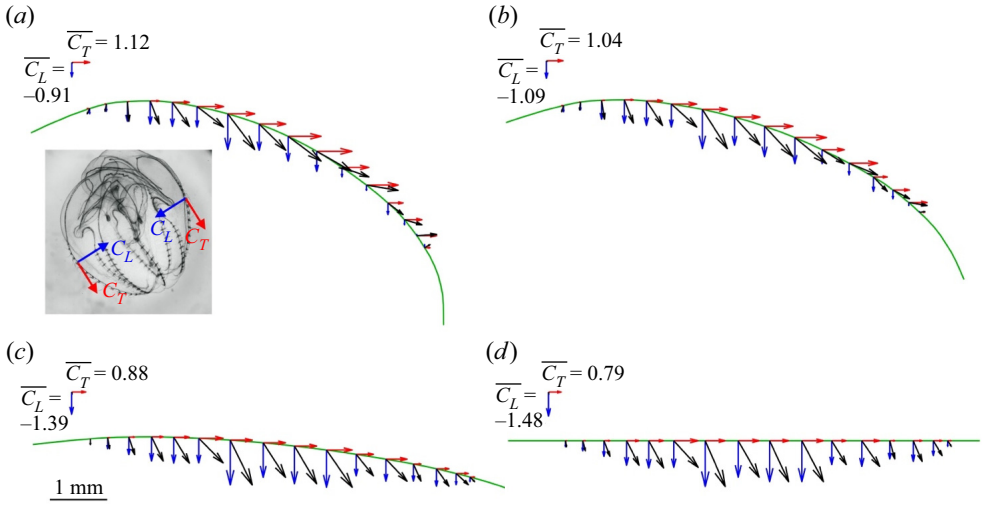

Figure 27. Vector diagram showing the average thrust (coloured red) and lift (coloured blue) produced by each ctene. Results are shown for different substrate curvatures, including (*a*) the original curvature, (*b*) medium curvature, (*c*) low curvature and (*d*) flat. Average ctene row force vectors are shown above each curvature. See movie in the supplementary material.

destructive tip vortex interactions are minimized during the thrust-producing power stroke and are maximized during the drag-producing recovery stroke. To quantify the effects of this vortex-weakening mechanism, we created an artificial 'sparse' simulation case in which the distance between ctenes is approximately doubled. Compared with the sparse case (in which vortex interactions are greatly reduced), we found that the vortex-weakening mechanism increases overall thrust production, decreases power consumption and increases the thrust-to-power ratio. In addition, we found that the performance of the vortex-weakening mechanism is dependent on the Reynolds number. As *Re* increases, tip vortices detach from the beating ctenes. Because the vortex-weakening mechanism is caused by interactions between ctene tip vortices, it becomes much less effective when tip vortices detach at higher *Re*. However, thrust-to-power ratio increases as *Re* increases, indicating that metachronal propulsion may be effective at higher *Re* as well as the low-to-intermediate *Re* at which it is typically observed. Additionally, the vortex-weakening mechanism may be extended to higher *Re* if ctene spacing is smaller, as observed in some ctenophore species.

In nature, ctenophores can possess a wide variety of different body morphologies. To determine how body geometry affects ctenes' performance and vortex interactions, we examined the hydrodynamics of ctenophore ctenes situated along substrates with different body curvatures. Our results show that if ctene kinematics are preserved and substrate curvature is decreased, overall thrust decreases and overall lift increases. This indicates that ctenophores most likely orient their ctenes and vary beating kinematics to maximize thrust production and minimize lift production across different curvatures/morphologies. In other words, ctene (and cilia) kinematics for a highly curved substrate are unlikely to be identical to those operating on a flatter substrate; this represents a promising direction for future study. We also demonstrated that the substrate curvature has little effect on the vortex-weakening mechanism, which indicates that this mechanism is effective across a variety of different body morphologies.

Ctene	Length (mm)	Aspect ratio (width/length)
a	0.266	3.887
b	0.330	3.127
c	0.523	1.975
d	0.541	1.910
e	0.534	1.935
f	0.568	1.818
g	0.645	1.602
h	0.647	1.597
i	0.697	1.482
j	0.682	1.514
k	0.617	1.676
l	0.652	1.584
m	0.559	1.848
n	0.532	1.942
o	0.437	2.365
p	0.191	5.408

Table 8. Length and aspect ratio of the model ctenes.

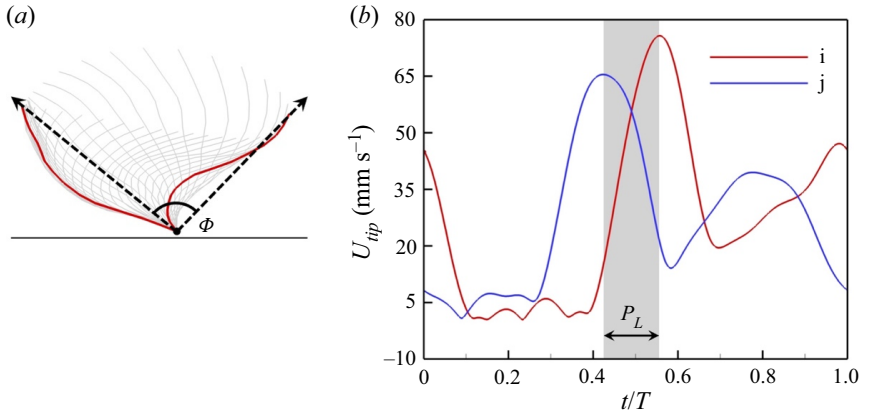

Figure 28. Images showing how (*a*) the stroke amplitude Φ and (*b*) the phase lag P_L were calculated.

In this study, we identified a new vortex-weakening mechanism that enhances the performance of metachronal rowing. Our findings suggest that there is an optimal relationship of morphological (e.g. appendage spacing) and kinematic (e.g. phase lag) parameters that maximizes the effectiveness of this mechanism. Further examination of this relationship could yield new insights into how metachronal rowing performs across different scales and species, as well as guide the development of bio-inspired swimming robots.

Supplementary movie. Supplementary movie is available at https://doi.org/10.1017/jfm.2023.739.

Acknowledgements. We thank E. Seber (Penn State), D. Murphy, F. Karakas and D. Olsen (University of South Florida) as well as A. Maass and A. Miccoli (BIOS) for assistance with data collection. All simulations were run on the High-Performance Computing Cluster of the College of Engineering at Villanova University.

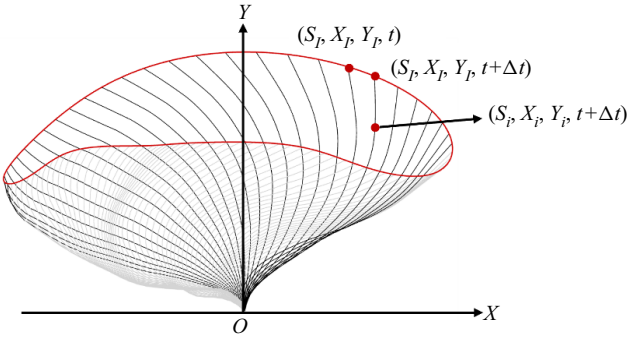

Figure 29. Illustration of the notation.

Funding. This research was supported by grants from the National Science Foundation to C.L. (NSF CBET-2120505) and to M.L.B. (NSF CBET-2120689), as well as a Grant-In-Aid (Samuel Riker Fellowship) from the Bermuda Institute of Ocean Sciences (BIOS).

Declaration of interests. The authors report no conflict of interest.

Author ORCIDs.
Seth Lionetti https://orcid.org/0009-0001-9276-8265;
Zhipeng Lou https://orcid.org/0009-0008-0421-9313;
Adrian Herrera-Amaya https://orcid.org/0000-0002-1901-2701;
Margaret L. Byron https://orcid.org/0000-0001-8012-078X;
Chengyu Li https://orcid.org/0000-0002-8379-2423.

Appendix A. Ctene dimensions

The length of each ctene in the model row matches the length of the real ctene in the high-speed video used for reconstruction. The width of the model ctenes is assumed to be constant, consistent with previous computational studies on metachronal rowing (Dauptain *et al.* 2008; Granzier-Nakajima *et al.* 2020). Although the actual ctenophore has slightly narrower ctenes near the end of the row compared with those in the middle, we assume this variation is minimal; width variation over the time course of the beat cycle for a single ctene (not accounted for in our model) is likely to be much more significant (Goebel *et al.* 2020), of the order of 30 % greater during the power stroke vs. the recovery stroke. Therefore, our simulations likely underestimate overall force production by an amount that is greater than that resulting from a systematic difference in ctene width. Furthermore, we believe that the constant width assumption does not significantly impact our study's overall conclusions. The length and aspect ratio of the model ctenes are recorded in table 8.

Appendix B. Calculation of stroke amplitude and phase lag

In this study, we define the stroke amplitude Φ as the angle traversed by the ctene tip during the power stroke. This definition is illustrated in figure 28(*a*), which shows a time sequence of a ctene's motion throughout its beating cycle. The positions of the ctene at the beginning and end of the power stroke are shown in red, and the stroke angle is measured between the ctene tips at these positions. We define the phase lag P_L between two neighbouring ctenes as the time difference between their respective moments of maximum tip velocity. This definition is shown in figure 28(*b*), which uses the tip velocities of ctenes 'i' and 'j' as a representative example.

		A_{mn} ($\times 10^{-3}$)				B_{mn} ($\times 10^{-3}$)		
	$n=$	0	1	2	3	1	2	3
				CTENE A				
$m=1$	x	−470.410	−156.160	115.860	−36.062	−36.463	82.802	−34.983
	y	63.542	−116.710	30.354	−7.186	−52.545	15.348	25.947
$m=2$	x	159.530	55.971	−115.520	37.497	−116.150	−2.801	24.254
	y	152.850	32.659	−8.252	−12.597	44.591	−1.161	−35.152
$m=3$	x	2.171	−0.792	0.511	0.811	−1.963	0.142	0.044
	y	1.181	0.989	−2.016	−2.395	−0.170	−1.160	−1.327
				CTENE B				
$m=1$	x	−595.700	−261.700	108.240	15.970	169.630	−106.780	87.798
	y	239.980	−74.673	−25.102	31.982	22.644	2.398	−16.631
$m=2$	x	387.920	26.618	−15.379	−51.115	−239.590	146.370	−63.097
	y	138.830	−15.158	24.700	−23.359	10.913	−41.643	21.568
$m=3$	x	7.773	−2.239	9.029	−4.176	−4.381	1.819	−0.602
	y	3.157	−2.377	−1.658	−0.121	1.560	−3.385	2.351
				CTENE C				
$m=1$	x	−1, 077.800	−93.430	−188.810	15.010	474.990	−160.580	−117.900
	y	451.100	−27.143	−18.522	−66.160	77.510	86.289	−24.008
$m=2$	x	742.660	−244.200	190.190	16.885	−361.010	65.039	131.030
	y	165.840	52.457	−20.966	75.200	−0.309	−78.832	6.188
$m=3$	x	4.855	11.972	−2.866	−3.636	−14.222	7.147	−0.136
	y	−3.072	1.277	1.577	2.788	−0.334	−3.370	2.238
				CTENE D				
$m=1$	x	−1077.800	−93.430	−188.810	15.010	361.970	181.750	22.350
	y	451.100	−27.143	−18.522	−66.160	71.057	87.443	111.320
$m=2$	x	742.660	−244.200	190.190	16.885	−40.983	−205.140	−62.903
	y	165.840	52.457	−20.966	75.200	−21.123	−44.253	−90.504
$m=3$	x	4.855	11.972	−2.866	−3.636	−12.970	5.307	5.187
	y	−3.072	1.277	1.577	2.788	2.047	−2.178	−2.455

Table 9. Fourier-least-squares coefficients for ctenes ‘a’–‘d’.

Appendix C. Ctene kinematics

To make our work replicable, we provide an approximate model of ctene kinematics using the Fourier-series-least-squares (FS-LS) method developed by Blake (1972). Since ctenes are modelled as rectangular membrane surfaces, we use the centreline in an XOY cross-sectional plane as a representation of the whole membrane. As shown in figure 29, the centreline of a certain single ctene is discretized into I pieces, where each point on the centreline is denoted by s_i ($i=0, 1, \ldots, I$), which measures the arclength from the ctene root. Since the reconstructed model gives the trajectory data of any arbitrary point i in one period in the form of the coordinates $X_i(s_i, t)$ and $Y(s_i, t)$, we can approximate these data along a time course using a Fourier series.

The truncated FS equation is given by (C1) and (C2)

$$X_i(s_i, t) = \frac{1}{2}a_{0,x}(s_i) + \sum_{n=1}^{N}\left[a_{n,x}(s_i)\cos\left(\frac{2n\pi}{T}t\right) + b_{n,x}(s_i)\sin\left(\frac{2n\pi}{T}t\right)\right], \tag{C1}$$

		A_{mn} ($\times 10^3$)				B_{mn} ($\times 10^3$)		
	$n=$	0	1	2	3	1	2	3
				CTENE E				
$m=1$	x	−1048.200	452.320	144.420	106.560	107.530	201.190	113.200
	y	538.170	97.599	46.262	38.774	−25.808	−22.427	−78.194
$m=2$	x	707.530	−281.310	−183.390	−127.300	255.480	−55.510	−50.958
	y	187.890	−29.644	13.257	−10.025	4.055	27.038	86.390
$m=3$	x	−3.656	−8.305	1.142	−0.538	−4.876	−6.884	−1.912
	y	−6.151	1.384	0.032	−2.397	4.102	2.530	1.568
				CTENE F				
$m=1$	x	−793.710	527.700	239.220	30.862	−196.970	2.927	−61.194
	y	607.770	117.400	−19.961	−82.099	1.401	−26.715	−15.229
$m=2$	x	545.950	−179.200	−138.630	43.850	417.600	103.720	79.465
	y	147.990	−66.476	58.894	104.860	−46.254	−24.903	−19.749
$m=3$	x	−11.516	−8.548	−4.157	−3.435	−7.801	−10.818	0.613
	y	−0.241	5.021	0.111	0.944	2.069	7.868	5.985
				CTENE G				
$m=1$	x	−1133.100	205.990	−126.820	−163.890	−553.000	−315.550	−35.413
	y	610.350	−30.851	−130.010	48.109	−180.700	15.472	113.200
$m=2$	x	764.690	207.930	251.840	134.080	441.780	199.320	−23.803
	y	183.910	9.327	78.637	−65.495	124.600	−17.179	−87.319
$m=3$	x	29.065	−12.707	−6.351	1.607	13.046	8.246	6.360
	y	11.315	5.441	1.132	−3.365	−1.953	−3.255	−3.134
				CTENE H				
$m=1$	x	−1164.200	−246.740	−317.630	52.734	−582.930	−16.196	−5.039
	y	527.900	−4.599	60.353	−3.864	−109.980	110.280	−89.131
$m=2$	x	772.090	484.830	216.390	−87.816	174.170	−146.830	36.089
	y	277.530	−37.158	−73.957	47.024	82.535	−47.907	89.085
$m=3$	x	−10.789	0.545	8.183	−4.766	14.192	16.051	0.308
	y	−5.877	−4.669	−3.993	0.352	1.401	−7.743	3.649

Table 10. Fourier-least-squares coefficients for ctenes ‘e’–‘h’.

$$Y_i(s_i, t) = \frac{1}{2}a_{0,y}(s_i) + \sum_{n=1}^{N}\left[a_{n,y}(s_i)\cos\left(\frac{2n\pi}{T}t\right) + b_{n,y}(s_i)\sin\left(\frac{2n\pi}{T}t\right)\right], \tag{C2}$$

where T is the beating period and N represents the number of terms in the FS. Here, $a_{0,x}(s_i)$, $a_{n,x}(s_i)$ and $b_{n,x}(s_i)$ are the FS coefficients in the x direction obtained from the known trajectory, and $a_{0,y}(s_i)$, $a_{n,y}(s_i)$ and $b_{n,y}(s_i)$ are the coefficients in the y direction. Then, the resulting coefficients are fitted into polynomial equations using the linear least-squares method in (C3) and (C4)

$$a_{n,x}(s_i) = \sum_{m=1}^{M} A_{mn,x}s^m, \quad b_{n,x}(s_i) = \sum_{m=1}^{M} B_{mn,x}s^m, \tag{C3a,b}$$

$$a_{n,y}(s_i) = \sum_{m=1}^{M} A_{mn,y}s^m, \quad b_{n,y}(s_i) = \sum_{m=1}^{M} B_{mn,y}s^m, \tag{C4a,b}$$

		A_{mn} ($\times 10^3$)				B_{mn} ($\times 10^3$)		
	$n=$	0	1	2	3	1	2	3
				CTENE I				
$m=1$	x	−1325.400	−598.400	44.068	−76.968	−364.480	289.800	−100.790
	y	565.730	−135.510	74.396	−68.738	50.676	−53.105	77.542
$m=2$	x	941.540	503.830	−193.080	117.900	−109.710	−206.900	60.148
	y	254.170	81.371	0.954	69.328	−16.580	90.262	−101.810
$m=3$	x	10.831	16.359	4.231	−3.388	12.811	−11.465	4.241
	y	1.586	0.370	1.873	0.832	−4.838	2.748	−2.259
				CTENE J				
$m=1$	x	−1408.400	−591.740	249.280	−164.390	144.130	−91.389	159.670
	y	577.150	−15.260	−98.037	191.120	129.100	−121.540	−38.662
$m=2$	x	977.440	193.020	−178.220	70.844	−418.900	200.970	−159.230
	y	242.690	9.273	135.790	−177.200	−63.973	61.621	62.728
$m=3$	x	12.423	14.825	−16.298	9.896	−3.739	−1.032	−7.144
	y	−5.532	−8.153	4.845	−5.060	1.340	0.922	3.887
				CTENE K				
$m=1$	x	−975.380	−429.340	−110.830	9.241	597.240	−270.790	−27.914
	y	647.710	50.367	8.224	−28.630	53.995	40.364	−37.065
$m=2$	x	766.630	−40.373	186.040	−15.631	−532.700	193.790	48.522
	y	148.370	−6.954	−28.685	68.369	−0.535	−61.069	44.420
$m=3$	x	−3.745	10.188	−9.722	−1.863	−11.794	14.779	0.282
	y	−5.223	−4.658	1.287	4.050	−0.445	−4.775	1.586
				CTENE L				
$m=1$	x	−1292.600	14.495	−315.720	−42.536	647.500	−41.843	−131.810
	y	584.150	85.248	−17.113	2.550	51.259	42.613	76.418
$m=2$	x	944.360	−370.910	255.820	65.798	−349.900	−74.866	101.600
	y	189.790	−17.573	−22.443	−7.960	−8.154	−15.480	−92.551
$m=3$	x	7.584	4.236	10.225	−5.365	−27.631	12.107	11.483
	y	0.850	−1.712	2.980	0.950	3.300	0.317	−2.944

Table 11. Fourier-least-squares coefficients for ctenes 'i'−'l'.

where $A_{mn,x}$ and $B_{mn,x}$ are the polynomial coefficients in the x direction, and $A_{mn,y}$ and $B_{mn,y}$ are the coefficients in the y direction. Once we solve for the polynomial coefficients, we can derive the kinematics model by substituting (C3) and (C4) into (C1) and (C2). Thus, the FS-LS model yields (C5) and (C6)

$$X_i(s_i, t) = \frac{1}{2}\sum_{m=1}^{M} A_{m0,x} s^m + \sum_{n=1}^{N}\left[\sum_{m=1}^{M}\left[A_{mn,\,x} s^m \cos\left(\frac{2n\pi}{T}t\right)\right] + \sum_{m=1}^{M}\left[B_{mn,x} s^m \sin\left(\frac{2n\pi}{T}t\right)\right]\right], \tag{C5}$$

$$Y_i(s_i, t) = \frac{1}{2}\sum_{m=1}^{M} A_{m0,y} s^m + \sum_{n=1}^{N}\left[\sum_{m=1}^{M}\left[A_{mn,y} s^m \cos\left(\frac{2n\pi}{T}t\right)\right] + \sum_{m=1}^{M}\left[B_{mn,y} s^m \sin\left(\frac{2n\pi}{T}t\right)\right]\right], \tag{C6}$$

		A_{mn} ($\times 10^3$)				B_{mn} ($\times 10^3$)		
	$n=$	0	1	2	3	1	2	3
				CTENE M				
$m=1$	x	−1011.200	342.900	−127.900	−1.137	319.050	158.380	73.167
	y	559.890	10.605	47.412	61.539	92.799	−28.183	−1.243
$m=2$	x	711.520	−475.910	52.834	−58.368	66.766	−172.210	−54.747
	y	96.809	35.541	−0.971	−54.593	−73.332	44.513	12.274
$m=3$	x	−1.360	3.157	8.785	−2.126	−21.603	−4.802	−4.911
	y	−2.162	3.582	−1.838	0.189	−3.953	2.561	−0.200
				CTENE N				
$m=1$	x	−932.110	553.850	131.510	47.669	66.209	112.270	43.306
	y	531.420	21.588	92.422	53.111	75.965	−25.250	−0.729
$m=2$	x	654.510	−460.960	−165.170	−54.805	280.530	−49.271	17.591
	y	141.690	51.665	−3.413	−2.028	−95.786	15.808	1.559
$m=3$	x	−0.171	−4.666	−6.368	−3.895	−7.533	−11.486	−6.351
	y	−10.120	5.199	−3.664	−4.777	−7.764	5.449	−0.530
				CTENE O				
$m=1$	x	−577.920	585.600	147.400	39.458	−292.450	25.274	−23.989
	y	514.720	−26.418	37.644	−48.564	111.710	−61.732	1.873
$m=2$	x	478.050	−306.790	−56.543	12.396	438.500	3.288	17.343
	y	−28.684	7.155	−30.281	43.370	−174.220	−7.961	−6.433
$m=3$	x	10.099	−18.167	−5.185	−2.171	4.711	−13.180	0.180
	y	1.779	8.362	2.575	5.871	−11.696	5.287	−2.266
				CTENE P				
$m=1$	x	−342.260	101.810	6.096	−14.916	−219.630	−62.530	−9.903
	y	287.230	39.793	1.755	−28.387	4.830	35.873	8.761
$m=2$	x	274.180	61.321	14.930	−4.060	190.460	54.678	−1.036
	y	−51.693	−74.979	−22.612	15.479	−13.024	−55.219	−2.210
$m=3$	x	1.061	1.050	0.047	−1.427	0.415	2.077	−0.428
	y	4.000	2.549	−1.035	0.048	1.873	1.808	1.219

Table 12. Fourier-least-squares coefficients for ctenes ‘m’–‘p’.

where the number of FS terms is $N=3$ and the number of polynomial terms is $M=3$.

Tables 9–12 summarize the values of the coefficients A_{mn} and B_{mn} for the x and y directions, which represent the approximate models of ctenes ‘a’–‘p’. To replicate the kinematics of the reconstructed model in our simulations, the readers can discretize their centreline model into arbitrary pieces and calculate the arclength from the root for each point. Then, input the provided coefficients into (C5) and (C6) to calculate coordinates of each point at any time instance within one beating period.

Appendix D. Validation of computational modelling

To validate the CFD solver used in the current study, we calculated the power output of each ctene using the method described by Barlow & Sleigh (1993). In this previous study, the authors estimated a ctenophore’s power output using the water jet produced by the beating ctenes. The peak power P in a water jet is defined as $P=\frac{1}{2}\rho u^3 A$, where ρ is the density of seawater (1027 kg m^{-3}), u is the peak flow speed within the jet and A is the cross-sectional area of the jet. The cross-sectional area A is approximated by

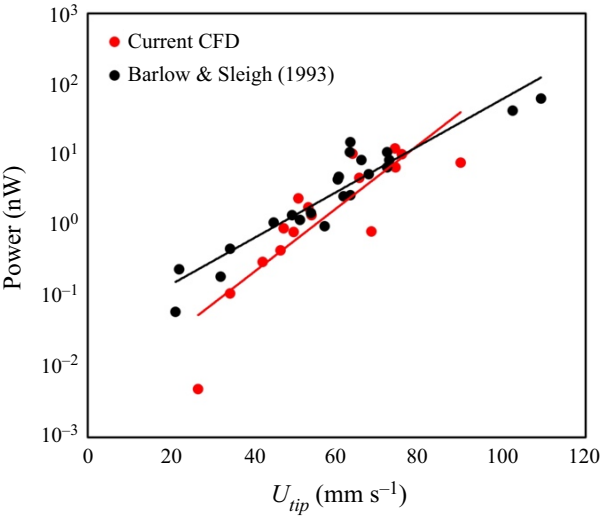

Figure 30. Plot showing the relationship between peak power output and peak ctene tip speed. Results from the current study are compared with results calculated by Barlow & Sleigh (1993). The data from each study are fitted using a least-squares exponential trendline.

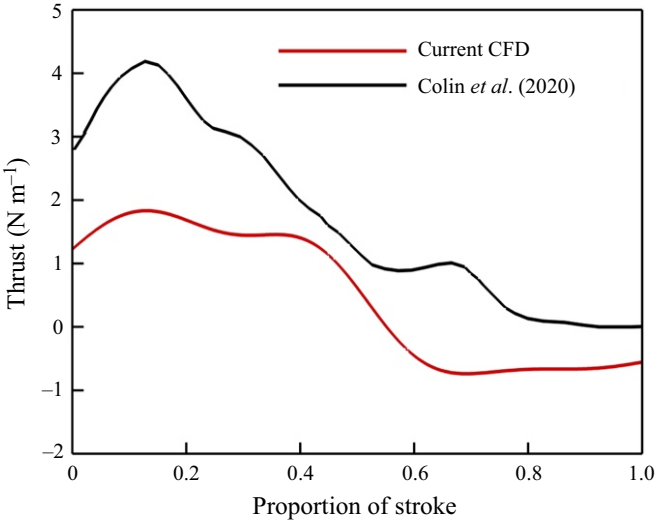

Figure 31. Plot showing instantaneous thrust generated by a single ctene during its power stroke. Results from the current computational study are compared with experimental results obtained by Colin *et al.* (2020).

extending a line from the velocity contour corresponding to the peak flow u to the contour corresponding to $\sim$20 % u. This distance is treated as the radius of a cylindrical water jet.

Using the results from our CFD simulation, we replicated this process to estimate the peak power output of each of the sixteen model ctenes. Figure 30 compares the results from the current study with those obtained by Barlow & Sleigh (1993). In this figure, ctene power output is plotted as a function of peak tip speed. Our results agree reasonably well with the previous study, and both studies show that power output increases exponentially with tip speed.

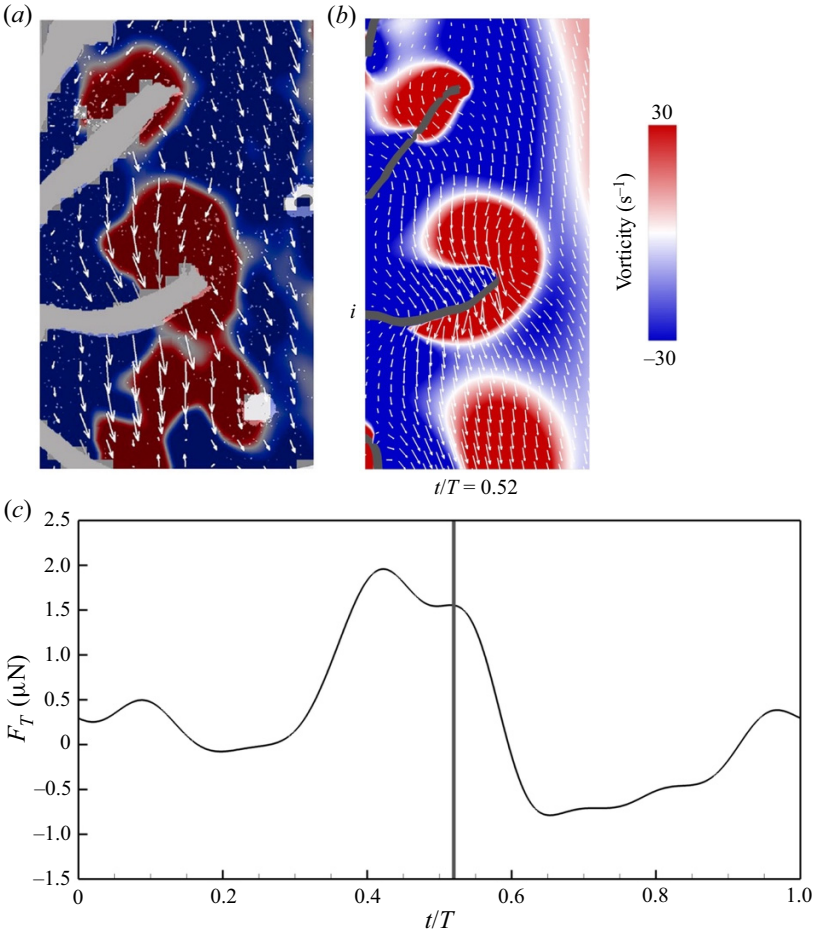

Figure 32. Comparison between vorticity results reported by (*a*) Colin *et al.* (2020) and obtained using (*b*) the current CFD solver. Velocity vectors are shown in white. The results from the current solver show the vorticity field around ctene 'i' (labelled) at $t/T = 0.52$. (*c*) Shows the real thrust generated by ctene 'i' at this particular time instant.

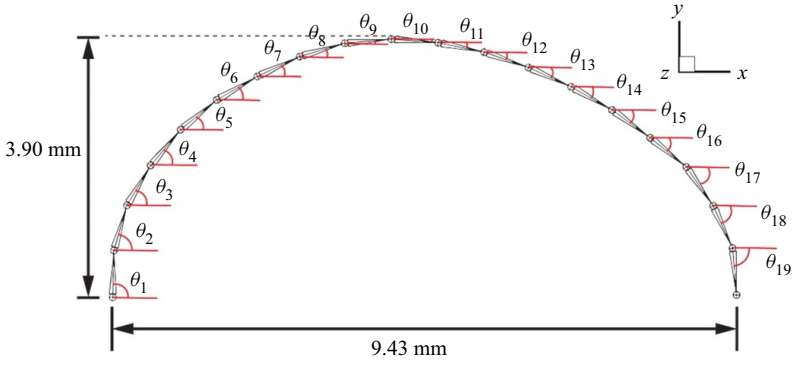

Figure 33. Schematic showing the skeleton structure of the model substrate created using Autodesk Maya. The skeleton is curved to match the body curvature of the real ctenophore.

	Original curvature (deg.)	Medium curvature (deg.)	Low curvature (deg.)	Flat (deg.)
θ_1	88.07	58.13	29.06	0.00
θ_2	74.19	48.97	24.48	0.00
θ_3	59.46	39.24	19.62	0.00
θ_4	50.25	33.17	16.58	0.00
θ_5	39.33	25.96	12.98	0.00
θ_6	29.88	19.72	9.86	0.00
θ_7	25.20	16.63	8.32	0.00
θ_8	16.47	10.87	5.44	0.00
θ_9	5.44	3.59	1.80	0.00
θ_{10}	−4.53	−2.99	−1.49	0.00
θ_{11}	−11.47	−7.57	−3.79	0.00
θ_{12}	−18.78	−12.39	−6.20	0.00
θ_{13}	−24.66	−16.28	−8.14	0.00
θ_{14}	−29.54	−19.50	−9.75	0.00
θ_{15}	−35.97	−23.74	−11.87	0.00
θ_{16}	−38.55	−25.44	−12.72	0.00
θ_{17}	−55.06	−36.34	−18.17	0.00
θ_{18}	−65.56	−43.27	−21.63	0.00
θ_{19}	−85.01	−56.11	−28.05	0.00

Table 13. Substrate controller angles for the original, medium curvature, low curvature and flat cases.

We also validated the solver by comparing the thrust generated by ctene ‘i’ with experimental results obtained by Colin *et al.* (2020). By considering the width of ctene ‘i’ (1.03 mm), we were able to approximate its thrust production per metre in the z-direction, yielding units of N m^{-1} consistent with the measurements in the previous study. Results for the thrust generated by a ctene during its power stroke are compared in figure 31. In general, both studies exhibit a similar overall trend, and thrust generation is of the same order of magnitude. However, the previous study displays a larger magnitude of thrust compared with our CFD results. The discrepancies of the thrust magnitude between our results and the previous experimental measurements could be explained by differences in ctenophore body size, swimming conditions or ctene morphology. Another potential reason for this discrepancy is that the previous study calculated thrust based on two-dimensional flow measurements, which potentially ignored certain three-dimensional flow phenomena such as the edge/tip vortices formed by a finite-aspect-ratio ctene. This could lead to an overestimation of thrust generation relative to our simulation.

In addition, we found that the vortex formed during the power stroke of ctene ‘i’ is comparable to results obtained by Colin *et al.* Figure 32(*a*,*b*) shows vorticity plots from the previous and current studies, respectively. Figure 32(*c*) shows the real thrust generated by ctene ‘i’ at the time instant when we observed this vortex formation.

To further prove the validity of our results, we also determined that the cycle-averaged total thrust produced by the model ctene row (2.42 μN) is sufficient to overcome the drag of a sphere with the same diameter as the ctenophore body examined in this study.

Appendix E. Modification of substrate curvature

To reconstruct the model substrate in Autodesk Maya, we created a discretized skeleton governed by a set of 19 controllers (shown in figure 33). The angle θ of each controller is defined as the angle between the skeleton and the positive X direction. To flatten the

model substrate, we reduced each controller angle by a common factor (66 % θ for the medium curvature case, 33 % θ for the low curvature case and 0 % θ for the flat case). The controller angles for the four different substrate curvatures are recorded in table 13. Ctenes and their accompanying kinematics were also rotated according to the prescribed angles.

References

Afzelius, B.R.A. 1961 The fine structure of the cilia from ctenophore swimming-plates. *J. Cell Biol.* **9** (2), 383–394.

Alben, S., Spears, K., Garth, S., Murphy, D. & Yen, J. 2010 Coordination of multiple appendages in drag-based swimming. *J. R. Soc. Interface* **7** (52), 1545–1557.

Barlow, D. & Sleigh, M.A. 1993 Water propulsion speeds and power output by comb plates of the ctenophore Pleurobrachia pileus under different conditions. *J. Exp. Biol.* **183** (1), 149–164.

Barlow, D., Sleigh, M.A. & White, R.J. 1993 Water flows around the comb plates of the ctenophore Pleurobrachia plotted by computer: a model system for studying propulsion by antiplectic metachronism. *J. Exp. Biol.* **177** (1), 113–128.

Blake, J. 1972 A model for the micro-structure in ciliated organisms. *J. Fluid Mech.* **55** (1), 1–23.

Byron, M.L., *et al.* 2021 Metachronal motion across scales: current challenges and future directions. *Integr. Compar. Biol.* **61** (5), 1674–1688.

Colin, S.P., Costello, J.H., Sutherland, K.R., Gemmell, B.J., Dabiri, J.O. & Du Clos, K.T. 2020 The role of suction thrust in the metachronal paddles of swimming invertebrates. *Sci. Rep.* **10** (1), 17790.

Dauptain, A., Favier, J. & Bottaro, A. 2008 Hydrodynamics of ciliary propulsion. *J. Fluids Struct.* **24** (8), 1156–1165.

Dong, H., Mittal, R., Bozkurttas, M., Lauder, G.V. & Madden, P. 2010 Computational modeling and analysis of the hydrodynamics of a highly deformable fish pectoral fin. *J. Fluid Mech.* **645**, 345–373.

Elgeti, J. & Gompper, G. 2013 Emergence of metachronal waves in cilia arrays. *Proc. Natl Acad. Sci.* **110** (12), 4470–4475.

Ford, M.P. & Santhanakrishnan, A. 2021*a* Closer appendage spacing augments metachronal swimming speed by promoting tip vortex interactions. *Integr. Compar. Biol.* **61** (5), 1608–1618.

Ford, M.P. & Santhanakrishnan, A. 2021*b* On the role of phase lag in multi-appendage metachronal swimming of euphausiids. *Bioinspir. Biomim.* **16** (6), 066007.

Garayev, K. & Murphy, D.W. 2021 Metachronal swimming of mantis shrimp: kinematics and interpleopod vortex interactions. *Integr. Compar. Biol.* **61** (5), 1631–1643.

Gibbons, M.J., Haddock, S.H., Matsumoto, G.I. & Foster, C. 2021 Records of ctenophores from South Africa. *PeerJ* **9**, e10697.

Goebel, W.L.H., Colin, S.P., Costello, J.H., Gemmell, B.J. & Sutherland, K.R. 2020 Scaling of ctenes and consequences for swimming performance in the ctenophore Pleurobrachia bachei. *Invertebr. Biol.* **139** (3), e12297.

Goldstein, D., Handler, R. & Sirovich, L. 1993 Modeling a no-slip flow boundary with an external force field. *J. Comput. Phys.* **105** (2), 354–366.

Gopalkrishnan, R., Triantafyllou, M.S., Triantafyllou, G.S. & Barrett, D. 1994 Active vorticity control in a shear flow using a flapping foil. *J. Fluid Mech.* **274**, 1–21.

Granzier-Nakajima, S., Guy, R.D. & Zhang-Molina, C. 2020 A numerical study of metachronal propulsion at low to intermediate Reynolds numbers. *Fluids* **5** (2), 86.

Gueron, S. & Levit-Gurevich, K. 1999 Energetic considerations of ciliary beating and the advantage of metachronal coordination. *Proc. Natl Acad. Sci.* **96** (22), 12240–12245.

Herrera-Amaya, A., & Byron, M. 2023 Metachronal coordination enables omnidirectional swimming via spatially distributed propulsion. bioRxiv:2023.01.23.525300.

Herrera-Amaya, A., Seber, E.K., Murphy, D.W., Patry, W.L., Knowles, T.S., Bubel, M.M., Maas, A.E. & Byron, M.L. 2021 Spatiotemporal asymmetry in metachronal rowing at intermediate Reynolds numbers. *Integr. Compar. Biol.* **61** (5), 1579–1593.

Jeong, J. & Hussain, F. 1995 On the identification of a vortex. *J. Fluid Mech.* **285**, 69–94.

Karakas, F., Maas, A.E. & Murphy, D.W. 2020 A novel cylindrical overlap-and-fling mechanism used by sea butterflies. *J. Exp. Biol.* **223** (15), 221499.

Khaderi, S., Den Toonder, J. & Onck, P. 2011 Microfluidic propulsion by the metachronal beating of magnetic artificial cilia: a numerical analysis. *J. Fluid Mech.* **688**, 44–65.

KIM, D. & GHARIB, M. 2011 Characteristics of vortex formation and thrust performance in drag-based paddling propulsion. *J. Exp. Biol.* **214** (13), 2283–2291.
KIM, J., KIM, D. & CHOI, H. 2001 An immersed-boundary finite-volume method for simulations of flow in complex geometries. *J. Comput. Phys.* **171** (1), 132–150.
KNIGHT-JONES, E. 1954 Relations between metachronism and the direction of ciliary beat in Metazoa. *J. Cell Sci.* **3** (32), 503–521.
LEI, M., CRIMALDI, J. P., & LI, C. 2021 Navigation in odor plumes: How do the flapping kinematics modulate the odor landscape? *AIAA paper* 2021-2817.
LEI, M. & LI, C. 2020 The aerodynamic performance of passive wing pitch in hovering flight. *Phys. Fluids* **32** (5), 051902.
LI, C. 2021 Effects of wing pitch kinematics on both aerodynamic and olfactory functions in an upwind surge. *Proc. Inst. Mech. Engrs C: J. Mech. Engng Sci.* **235** (2), 296–307.
LI, C. & DONG, H. 2016 Three-dimensional wake topology and propulsive performance of low-aspect-ratio pitching-rolling plates. *Phys. Fluids* **28** (7), 071901.
LI, C. & DONG, H. 2017 Wing kinematics measurement and aerodynamics of a dragonfly in turning flight. *Bioinspir. Biomim.* **12** (2), 026001.
LI, C., DONG, H. & CHENG, B. 2020 Tip vortices formation and evolution of rotating wings at low Reynolds numbers. *Phys. Fluids* **32** (2), 021905.
LI, C., DONG, H. & LIU, G. 2015 Effects of a dynamic trailing-edge flap on the aerodynamic performance and flow structures in hovering flight. *J. Fluids Struct.* **58**, 49–65.
LI, C., DONG, H. & ZHAO, K. 2018 A balance between aerodynamic and olfactory performance during flight in Drosophila. *Nat. Commun.* **9** (1), 1–8.
LI, C., DONG, H. & ZHAO, K. 2020 Dual functions of insect wings in an odor-guided aeronautic navigation. *J. Fluids Engng* **142** (3), 030902.
LI, C., JIANG, J., DONG, H. & ZHAO, K. 2017 Computational modeling and validation of human nasal airflow under various breathing conditions. *J. Biomech.* **64** (7), 59–68.
LI, C., WANG, J., LIU, G., DENG, X. & DONG, H. 2019 Passive pitching mechanism of three-dimensional flapping wings in hovering flight, San Francisco, CA, USA (ASME 2019) V002T02A043. In *Proceedings of the 8th Joint Fluids Engineering Conference on ASME-JSME-KSME 2019*, AJKFluids 2019-4639.
LIM, J.L. & DEMONT, M.E. 2009 Kinematics, hydrodynamics and force production of pleopods suggest jet-assisted walking in the American lobster (Homarus americanus). *J. Exp. Biol.* **212** (17), 2731–2745.
LIONETTI, S., HEDRICK, T.L. & LI, C. 2022 Aerodynamic explanation of flight speed limits in hawkmoth-like flapping-wing insects. *Phys. Rev. Fluids* **7** (9), 093104.
LÖHNER, R. 2008 *Applied Computational Fluid Dynamics Techniques: An Introduction based on Finite Element Methods*. John Wiley & Sons.
MATSUMOTO, G. 1991 Swimming movements of ctenophores, and the mechanics of propulsion by ctene rows. *Hydrobiologia*. **216**, 319–325.
MILANA, E., ZHANG, R., VETRANO, M.R., PEERLINCK, S., DE VOLDER, M., ONCK, P.R., REYNAERTS, D. & GORISSEN, B. 2020 Metachronal patterns in artificial cilia for low Reynolds number fluid propulsion. *Sci. Adv.* **6** (49), eabd2508.
MITTAL, R., DONG, H., BOZKURTTAS, M., NAJJAR, F.M., VARGAS, A. & VON LOEBBECKE, A. 2008 A versatile sharp interface immersed boundary method for incompressible flows with complex boundaries. *J. Comput. Phys.* **227** (10), 4825–4852.
MITTAL, R. & IACCARINO, G. 2005 Immersed boundary methods. *Annu. Rev. Fluid Mech.* **37**, 239–261.
MURPHY, D., WEBSTER, D., KAWAGUCHI, S., KING, R. & YEN, J. 2011 Metachronal swimming in Antarctic krill: gait kinematics and system design. *Mar. Biol.* **158** (11), 2541–2554.
PESKIN, C.S. 1972 Flow patterns around heart valves: A numerical method. *J. Comput. Phys.* **10** (2), 252–271.
PRATT, V. 1987 Direct least-squares fitting of algebraic surfaces. *ACM SIGGRAPH Comput. Graph.* **21** (4), 145–152.
SLEIGH, M.A. 1976 Fluid propulsion by cilia and the physiology of ciliary systems. In *Perspectives in Experimental Biology, Volume 1: Zoology* (ed. P.S. Davies), pp. 125–134. Oxford: Pergamon Press.
TAIRA, K. & COLONIUS, T. 2007 The immersed boundary method: A projection approach. *J. Comput. Phys.* **225** (2), 2118–2137.
TAKAGI, D. 2015 Swimming with stiff legs at low Reynolds number. *Phys. Rev.* E **92** (2), 023020.
TAMM, S.L. 2014 Cilia and the life of ctenophores. *Invertebr. Biol.* **133** (1), 1–46.
TEZDUYAR, T.E. 2004 Finite element methods for fluid dynamics with moving boundaries and interfaces. In *Encyclopedia of Computational Mechanics* (ed. E. Stein, R. De Borst & T.J.R. Hughes). Vol. 3. Chap. 17. Wiley.

TEZDUYAR, T.E., SATHE, S., KEEDY, R. & STEIN, K. 2006 Space–time finite element techniques for computation of fluid–structure interactions. *Comput. Meth. Appl. Mech. Engng* **195** (17–18), 2002–2027.

VISBAL, M.R. & GAITONDE, D.V. 2001 Very high-order spatially implicit schemes for computational acoustics on curvilinear meshes. *J. Comput. Acoust.* **9** (04), 1259–1286.

VISBAL, M.R. & GAITONDE, D.V. 2002 On the use of higher-order finite-difference schemes on curvilinear and deforming meshes. *J. Comput. Phys.* **181** (1), 155–185.

VISBAL, M.R. & RIZZETTA, D. 2002 Large-eddy simulation on curvilinear grids using compact differencing and filtering schemes. *J. Fluids Engng* **124** (4), 836–847.

YE, T., MITTAL, R., UDAYKUMAR, H.S. & SHYY, W. 1999 An accurate cartesian grid method for viscous incompressible flows with complex immersed boundaries. *J. Comput. Phys.* **156** (2), 209–240.

ZHANG, P., JANA, S., GIARRA, M., VLACHOS, P. & JUNG, S. 2015 Paramecia swimming in viscous flow. *Eur. Phys. J. Spec. Top.* **224** (17), 3199–3210.

ZHANG, R., DEN TOONDER, J. & ONCK, P. R. 2021. Transport and mixing by metachronal waves in nonreciprocal soft robotic pneumatic artificial cilia at low Reynolds numbers. *Phy. Fluids* **33** (9), 092009.

ZHANG, R., DEN TOONDER, J. & ONCK, P.R. 2022 Metachronal patterns by magnetically-programmable artificial cilia surfaces for low Reynolds number fluid transport and mixing. *Soft Matter* **18** (20), 3902–3909.